Marine and Petroleum Geology 173 (2025) 107284

Contents lists available at ScienceDirect

Marine and Petroleum Geology

journal homepage: www.elsevier.com/locate/marpetgeo

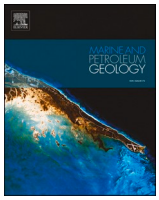

Recognition and impact on reservoir quality of fractures in fine-grained sedimentary rocks using image and array acoustic logs

Yuyue Huang [a,b,*], Guiwen Wang [a,b,**], Lichun Kuang [a,b], Chaoliu Li [c], Ming Wang [c], Song Wang [a,b], Hongbin Li [a,b], Fei Zhao [a,b], Jin Lai [a,b]

[a] National Key Laboratory of Petroleum Resources and Engineering, China University of Petroleum (Beijing), Beijing, 102249, China
[b] College of Geosciences, China University of Petroleum (Beijing), Beijing, 102249, China
[c] Research Institute of Petroleum Exploration and Development, PetroChina, Beijing, 100083, China

ARTICLE INFO

Keywords:
Fractures
Image logs
Array acoustic logs
Reservoir quality
Fine-grained sedimentary rocks
Ordos basin

ABSTRACT

Fine-grained sedimentary rocks have been widely regarded as effective reservoirs and source rocks of tight oil and shale oil. Natural fractures play a critical role in promoting oil enrichment and enhancing production. Clarifying the contribution of fractures to reservoir quality is important but lacks systematic research. Limitations exist in both core outcrop descriptions and seismic predictions of fractures. New technological advancements in well logs offer new avenues for multi-scale fracture characterization. Image logs and array acoustic logs are used to systematically investigate natural fractures in the Member 7 of Upper Triassic Yanchang Formation (Chang 7) shale oil reservoirs in the Ordos Basin. Natural fractures include tectonic fractures and bedding-parallel fractures. An absolute match between core data and image log data is achieved through the precise core homing. The reliability of image logs is enhanced by establishing the fracture identification templates under the core scale. The Vp/Vs ratio, energy attenuation, waveform distortion, and S-wave slowness anisotropy of array acoustic logs are effective for detecting and predicting natural fractures around the borehole. The impact of natural fractures on reservoir quality is evaluated by considering fracture parameters, radial extension and their relationship with in-situ stress. The results show that combining the occurrence and type of fractures detected by image logs and the fracture extension state indicated by fast and slow S-wave radial variations, the effectiveness of fractures around the wellbore can be accurately evaluated. T_1-T_2 maps from 2D NMR logs also offer insights into the relationship between fractures and reservoir quality. Natural fractures that are nearly parallel to the direction of the in-situ SH_{max} have proven to be effective and significantly enhance hydrocarbon productivity. The research above may aid in optimizing sweet spot evaluation and stimulating shale oil production.

1. Introduction

Fine-grained sedimentary rocks have gained significant attention as effective reservoirs and source rocks of tight oil and shale oil in recent years, driven by increasing energy demands (Hughes, 2013; Zou et al., 2020). Unlike high-porosity rocks, fine-grained sedimentary rocks are characterized by poor physical properties and pronounced heterogeneity, which present substantial challenges to oil extraction (Jarvie, 2012; Jiang et al., 2023, 2024; Zhao et al., 2024). The presence and characteristics of natural fractures have been established as key factors in promoting high shale oil production (Curtis, 2002; Marghani et al., 2023). Effective natural fractures can improve reservoir quality and facilitate communication within artificial fracture networks during hydraulic fracturing (Gale et al., 2007; Yang et al., 2022). Consequently, recognizing natural fractures and evaluating their effectiveness in fine-grained sedimentary rocks are critical for optimizing production strategies (Gong et al., 2021; Xu et al., 2022).

Natural fractures are widespread in fine-grained sedimentary rocks, and their types and spatial distribution are generally considered to depend on mechanical deposition, diagenesis, tectonic activity, and in-situ stress field conditions (Zeng and Li, 2009; Anders et al., 2014; Zeng et al., 2023). Unlike marine fine-grained sediments, continental lacustrine fine-grained sedimentary rocks are typically thin and frequently interbedded (Liu et al., 2021; Kuang et al., 2022). The

* Corresponding author. China University of Petroleum-Beijing, 18 Fuxue Road, Changping, Beijing, 102249, China.
** Corresponding author. China University of Petroleum, Beijing, China.
E-mail addresses: hyy990924@163.com (Y. Huang), wanggw@cup.edu.cn (G. Wang).

https://doi.org/10.1016/j.marpetgeo.2025.107284
Received 8 October 2024; Received in revised form 26 December 2024; Accepted 2 January 2025
Available online 4 January 2025

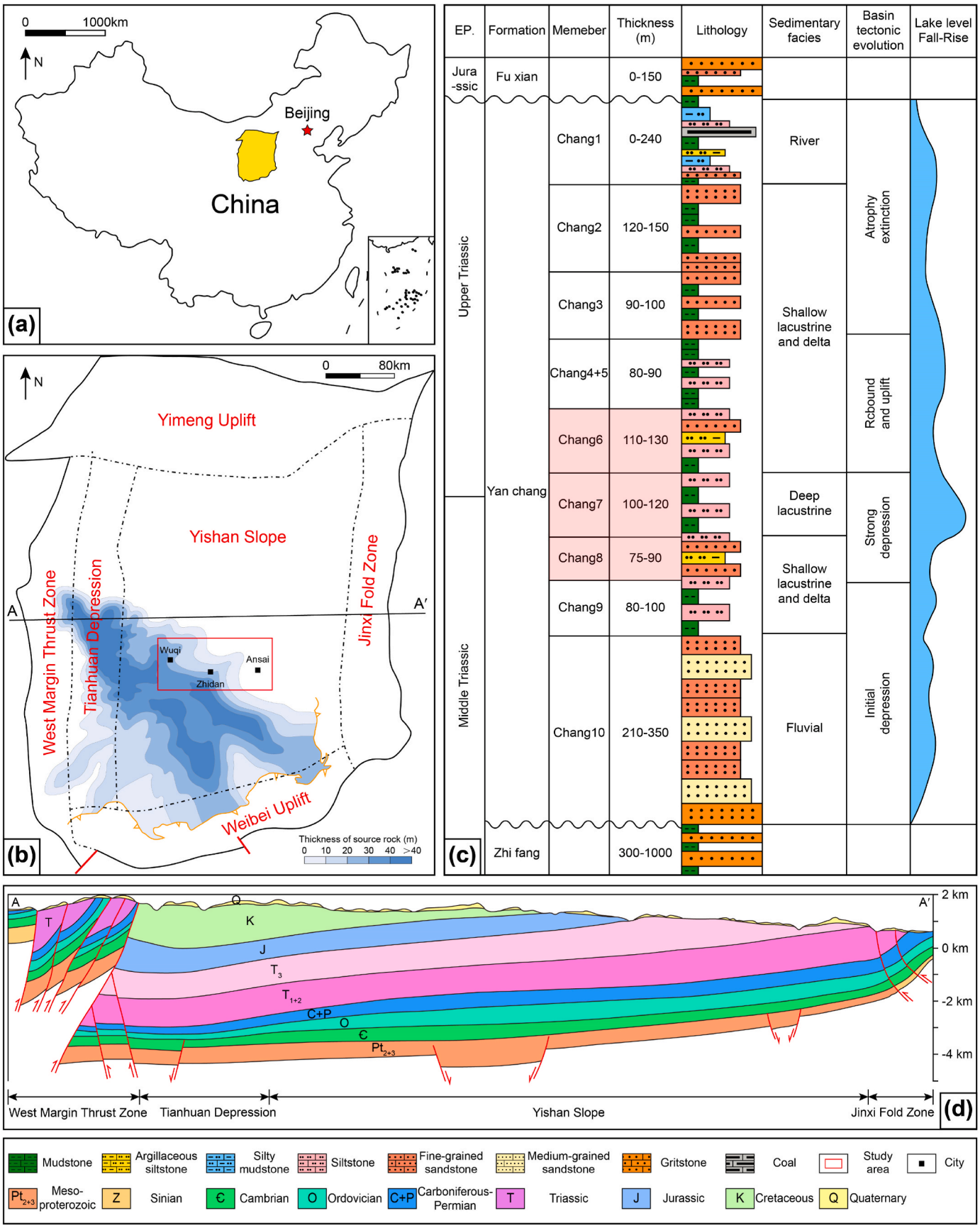

Fig. 1. (a). Location of the Ordos Basin in China. (b). Structure division of the Ordos Basin and the study area. (c). Stratigraphic column of Yanchang Formation in the Ordos Basin. (d). Structural cross-section of the Ordos Basin (He, 2022).

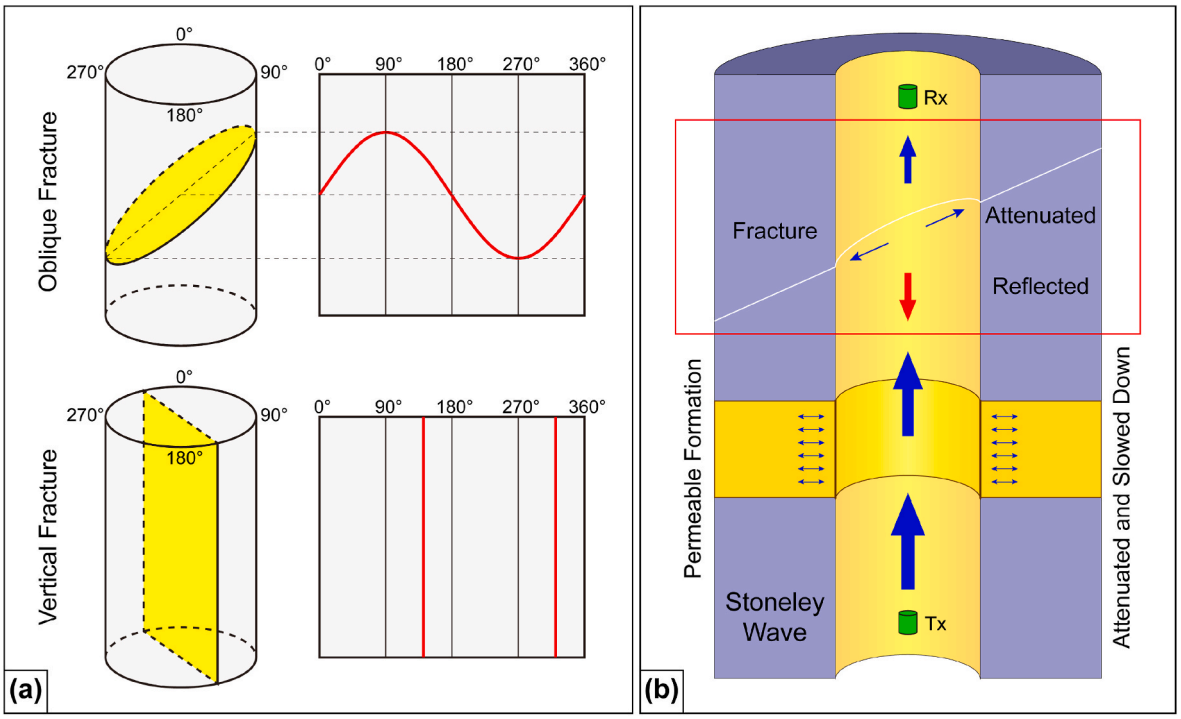

Fig. 2. Diagram of fracture detection using image logs and array acoustic logs. (a). The response characteristics of fractures with different occurrence by image logs. (b). Stoneley wave attenuation and reflection caused by permeable fractures.

presence of abundant sedimentary structures, such as laminae and bedding, leads to significant heterogeneity and anisotropy within the formation (Wang et al., 2021). The lamina planes or bedding interfaces are conducive to the formation of bedding-parallel fractures (Gale et al., 2014). These fractures can serve as both dominant storage spaces in fine-grained sedimentary rocks and critical seepage channels for shale oil (Loucks et al., 2012; Gou et al., 2019). Fluid migration and dissolution are likely to occur at the bedding interface of these mechanically weak laminae planes, thereby enhancing the effectiveness of bedding-parallel fractures (Hooker et al., 2017; Lai et al., 2022). Furthermore, the types and spatial distribution of natural fractures in lacustrine fine-grained sedimentary rocks vary significantly in different basins. The density of bedding-parallel fractures in the Qingshankou Formation in Gulong Sag of Songliao Basin can reach 1000/m, while the density of bedding-parallel fractures in Chang 7 Formation of Ordos Basin is several to dozens/m (Xi et al., 2020; Pang et al., 2023). However, there are differences in the formation and type of natural fractures controlled by tectonic action and in-situ stress even within the same basin. Abundant tectonic fractures are detected in the Fengcheng Formation shale of Mahu Sag (Huang et al., 2023), whereas the bedding-parallel fractures predominate in Lucaogou Formation of Jimusar Sag (Lai et al., 2022). They are both proved to contribute significantly to shale oil production and natural gas migration (Liu et al., 2009; Du et al., 2023a,b).

Focusing on natural fractures in the formation, multi-disciplinary geological and geophysical characterization techniques have been developed. According to the classification of natural fracture scale and research means, the current qualitative and quantitative characterization methods of natural fractures include: core scale fracture description, logging scale fracture recognition, and seismic scale fracture prediction (Tang et al., 2011; Boersma et al., 2020; Lai et al., 2023). Fracture characteristics such as morphology and dip angle can be directly observed through outcrop profile descriptions and core examinations (Strijker et al., 2012). The filling of microfractures can be analyzed using thin sections and SEM (Scanning Electron Microscope) (Gou et al., 2019). The relationship between microfractures and mineral cutting can be visually demonstrated by using micro-nano CT scanning (Wu et al., 2020; Chandra and Vishal, 2021). However, it is difficult to recognize the false fractures formed during the coring process. The fracture opening degree under in-situ stress state cannot be preserved by drilling coring. Currently, seismic coherence attributes and ant body tracking are the most effective methods for predicting the spatial distribution of fractures and faults (Wilson et al., 2015; Xu et al., 2018). However, their precision is relatively low. In contrast, well logs offer advantages such as continuous measurement, low cost, and high resolution. Logging characterization serves as a bridge from core scale to seismic scale (Donselaar and Schmidt, 2005; Lai et al., 2024). Image logs provide high-resolution visual representations of the borehole wall, enabling detailed detection of fractures, faults, and bedding planes (Canady et al., 2008). In particular, electrical image logs provide significant benefits in calculating fracture density, aperture, and porosity, which are critical parameters for evaluating fracture effectiveness (Aghli et al., 2020; Li et al., 2023a). Simultaneously, array acoustic logs have been extensively used for the recognition and evaluation of natural fractures (Haldorsen et al., 2006; Tang et al., 2011). By analyzing the travel time and attenuation of acoustic waves, the presence of fractures can be inferred (Hornby et al., 1989; Liu et al., 2023). The combination of image and array acoustic logs therefore provides a thorough method for fracture characterization (Tang et al., 2016; Lai et al., 2017). Furthermore, the high-resolution logging data quality and machine learning algorithms enhance the precision of fracture detection and characterization, thereby facilitating improved prediction of fractures in fine-grained sedimentary rocks (Lyu et al., 2019; Dong et al., 2024).

Despite the advancements and successes in fracture detection outlined above for sandstone and carbonate reservoirs, challenges remain in fracture recognition in fine-grained sedimentary rocks (Lai et al., 2021; Zeng et al., 2023). Image logs have been extensively used in fracture detection in fine-grained sedimentary rocks, there is limited research on the use of array acoustic logs for fracture prediction (Lai et al., 2017; Marghani et al., 2023). The evaluation of fracture effectiveness, particularly through the differences in detection depth and characteristics of image logs and array acoustic logs, has not been thoroughly

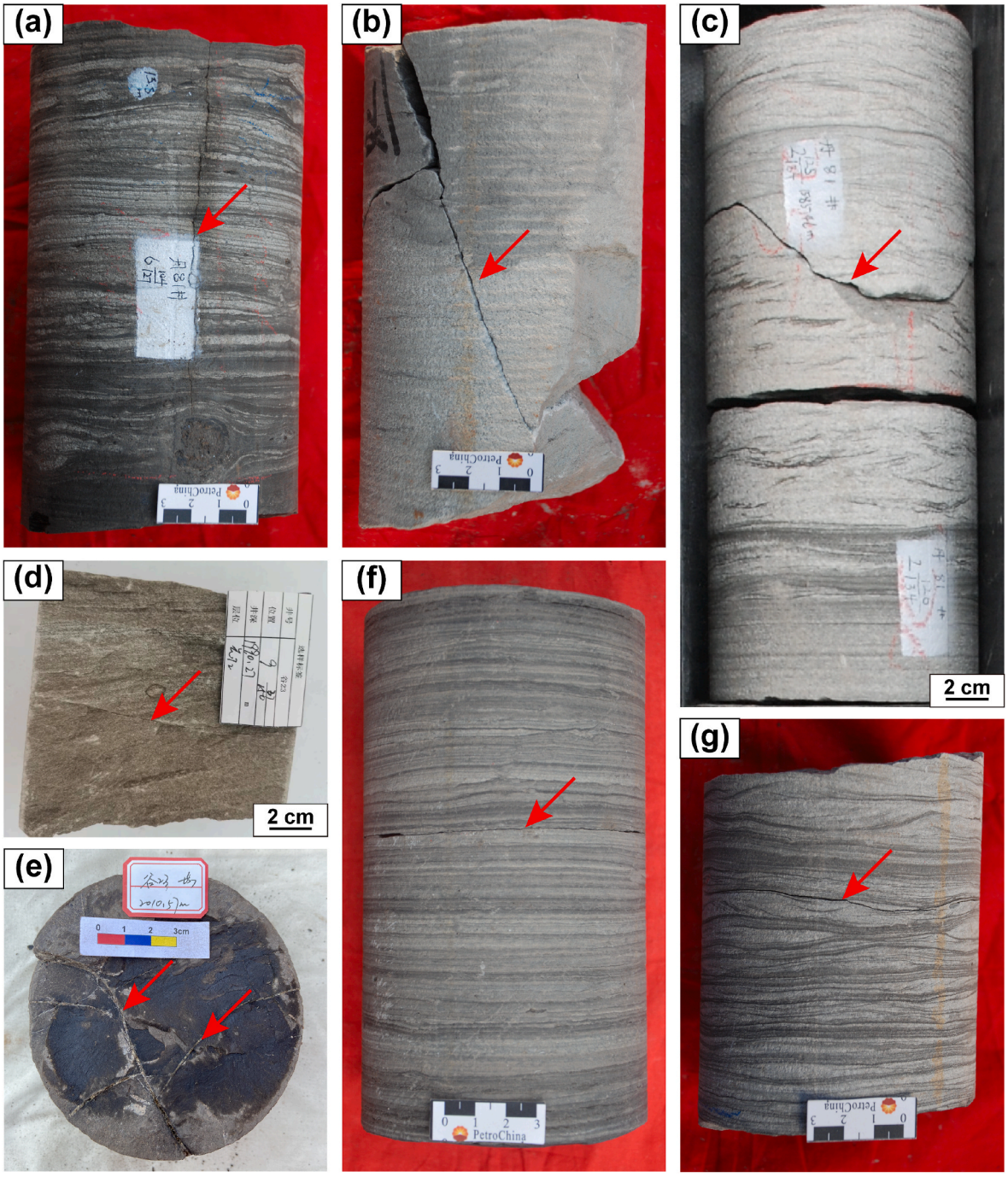

Fig. 3. Core photos show the types of natural fractures in fine-grained sedimentary rocks of the Ordos Basin. (a). Vertical fractures, Dan81, 1652.8m. (b). High-angle shear fractures, Dan81, 1602.0m. (c). Oblique shear fractures, Dan81, 1585.46m. (d). Low-angle shear fractures, Gu23, 1990.27m. (e). Fractures filled with calcite, Gu23, 2010.57m. (f). Bedding parallel fractures, Dan81, 1590.2m. (g). Bedding parallel fractures, Dan81, 1619.9m.

investigated (Tang et al., 2016; Liu et al., 2023; Lai et al., 2024). This study aims to address the critical aspects of fracture recognition, prediction, and its impact on reservoir quality in fine-grained sedimentary rocks by utilizing image and array acoustic logs. The objectives of this study are as follows: (1) to detect fractures through a combination of image logs and array acoustic logs; (2) to predict natural fractures around the borehole using the Vp/Vs ratio, energy attenuation, waveform distortion, and S-wave slowness anisotropy derived from array acoustic logs; (3) to evaluate the impact of natural fractures on reservoir quality through a combination of fracture parameters, radial extension, and their relationship with in-situ stress. Finally, the effect of fracture on hydrocarbon productivity in fine-grained sedimentary rocks can be revealed. The aim of this study is to systematically clarify the application of image logs and array acoustic logs in evaluating natural fractures in fine-grained sedimentary rocks. The results of the study are expected to provide a reference for the best practice in evaluating fracture effectiveness and stimulating shale oil production.

2. Geological setting

The Ordos Basin is located in the western part of the North China Craton, covering a total area of approximately 37 × 10^4 km^2. It is a typical inland basin with multiple superimposed cycles in northwestern China (Fig. 1a). The basin is bordered by the Lvliang Mountains to the

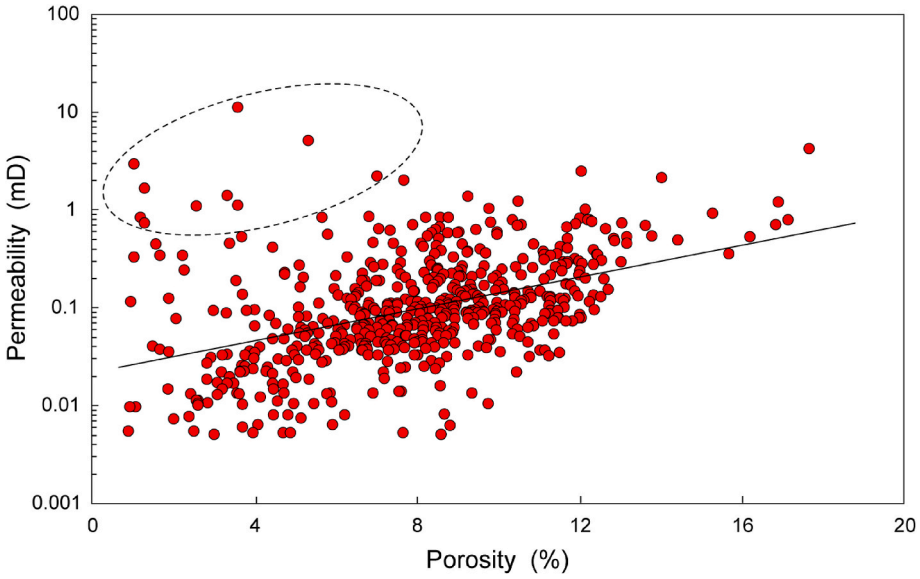

Fig. 4. Core-measured porosity and permeability of Yanchang Formation in the Ordos Basin.

east, Qinling orogenic belt to the south, Helan–Liupan Mountains to the west, and Yinshan orogenic belt to the north (Tian et al., 2024). Drawing upon its structural attributes, the Ordos Basin can be further divided into six secondary structural units: Weibei uplift, Yimeng uplift, Yishan slope, Jinxi fold zone, Tianhuan depression, and West margin thrust zone (Fu et al., 2020). The study area is located in the central part of the Yishang slope, extending to Ansai in the east, Zhidan in the south, and Wuqi in the west (Fig. 1b).

During the Late Triassic epoch, the lacustrine basin subsided and expanded rapidly due to the intense tectonic movement coupled with frequent seismic and volcanic activities. Deposits within the Ordos Basin changed from shallow-sea to lacustrine sedimentary facies. This transformation led to the accumulation of clastic depositional systems characterized by inland river-delta-lake facies (Guo et al., 2022; He, 2022). The Yanchang Formation represents a complete record of the origin, development, and extinction of a lake basin (Fig. 1c and d). According to rhythmic lithological variations and electric logging characteristics, the Yanchang Formation can be further divided into ten members, ranging from Chang 1 to Chang 10 from top to bottom. In the northern region, the total thickness of the Yanchang members is approximately 800–1000 m, gradually increasing to 1000–1400 m towards the south. According to the combination of lithology and sedimentary cycles, the Chang 7 Member can be subdivided into three units: Chang 7_1, Chang 7_2, and Chang 7_3, respectively. Chang 7_1 and Chang 7_2 are mainly composed of shale, siltstone, and fine sandstone, while Chang 7_3 is mostly composed of shale with a small amount of interbedded siltstone and fine sandstone. In summary, the Mesozoic Yanchang Formation in the Ordos Basin mainly comprises fine-grained sedimentary rocks such as semi-deep to deep lacustrine mudstone and shale. Meanwhile, The Chang 7 black shale has a great hydrocarbon generation and production potential, making it the major shale oil production layer in China (Guo et al., 2023).

3. Data and methods

A total of 5 key wells were observed for fractures on the drilled cores in this study. Special attentions were focused on the characteristics of tectonic fractures and bedding-parallel fractures. The fracture aperture, dip angle, filling material and filling degree were also examined.

Although it is the most intuitive method to observe fracture s through drilling cores, it is costly and consumes manpower and material resources. Well logs allow for continuous measurements and is widely used to detect petrophysical and other properties in downhole formations. The whole suite of conventional well logs includes gamma ray (GR), resistivity (RD, RS, and MSFL), density (DEN), neutron porosity (CNL), and acoustic time difference (AC) (Lai et al., 2017; Aghli et al., 2020). The response characteristics of fractures in conventional well logs typically include an increase in borehole diameter, an increase in acoustic travel time (sometimes accompanied by cycle skipping), a slight decrease in density, and a sharp, spike-like decrease in resistivity. These curves have different sensitivity to fracture response and can be used to constrain the location of fracture intervals (Lyu et al., 2016; Zhang et al., 2021).

Image logs are considered to be the most effective new logging technique for recogniting of various geological objects around wellbores (Canady et al., 2008). Image logs includes both electrical image logs and acoustic image logs. The Schlumberger's FMI (Fullbore Formation MicroImager), Haliborton's XRMI (Extended Range Micro Imager), and China National Logging Corporation's MCI (Micro-Conductivity Imager) electrical imaging tool was used to get high-resolution "pseudo-picture" of borehole walls. The complete borehole images can only be obtained by speed correction, eccentricity correction, static and dynamic normalization of the electrical image data (Donselaar and Schmidt, 2005; Wilson et al., 2015). Especially, FMI image logs have been widely used in the analysis of fine borehole structures due to its high longitudinal resolution (0.2 in or 5 mm) and high borehole coverage (80%). Natural fractures (near-vertical, inclined and bedding-parallel), which appeared as evident sinusoidal waves on the images (Fig. 2a). Acoustic image logs can measure the change of acoustic impedance of rock and perform 360° scan around the wellbore (Dewhurst et al., 2011). Instruments currently in use include Haliborton's CAST-V (Circumferential Acoustic Scanning Tool - Visualization), Schlumberger's UBL (Ultrasonic Borehole Imager), and Atlas's CBIL (Circumferential Borehole Imaging Log). These instruments such as have the advantages of greater detection depth (about 2 m) and better borehole coverage (100%) than the electrical image log tools. Acoustic image logs can not only be combined with electrical image logs to recognize fractures, but also can be used for casing detection and cement bond quality evaluation (Momeni et al., 2019).

Schlumberger's Sonic Scanner, DSI (dipole sonic imager), and Baker Hughes Company's XMAC are the three most commonly used array acoustic logs currently. XMAC log records full waveforms (amplitudes), and the compressional waves, shear waves, Stoneley waves can be extracted (Liu et al., 2023). Stoneley wave has a large radial detection

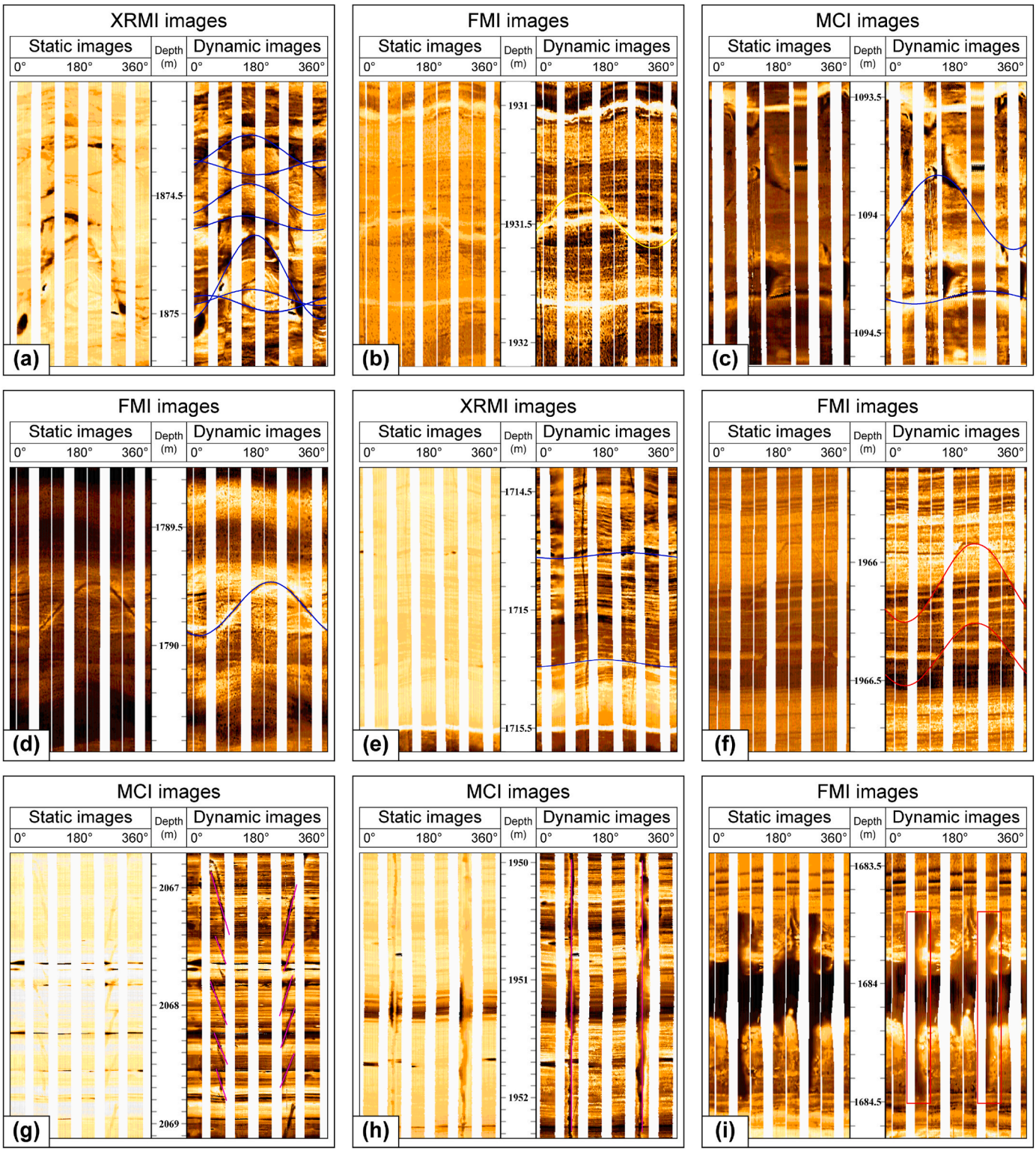

Fig. 5. Capture of various geological objects using image logs. (a). Network fractures picked out as blue sinusoidal curves. (b). Oblique resistive fractures picked out as yellow sinusoidal curves. (c). Oblique half-filled fractures picked out as blue sinusoidal curves. (d). Oblique conductive fractures picked out as blue sinusoidal curves. (e). Bedding parallel fractures appear as discontinuous sinusoidal curves. (f). Microfaults picked out as red sinusoidal curves. (g). En-echelon induced fractures picked out as short pink segments. (h). Vertical induced fractures picked out as long pink lines. (i). Borehole breakouts picked out as red regions. (For interpretation of the references to color in this figure legend, the reader is referred to the Web version of this article.)

depth, and its reflection attenuation mainly occurs in the intervals with good permeability (Tang et al., 2007). When there is a natural fracture in the formation that intersects with the borehole, Stoneley wave energy is lost due to the flow of mud in the well and fluid in the formation (Hornby et al., 1989; Lee et al., 2019). And the reflected Stoneley wave is formed at the depth of the fracture. Therefore, Stoneley wave energy attenuation and interference fringe features of full-wave series varied-density images can recognize and predict natural fractures around wellbores

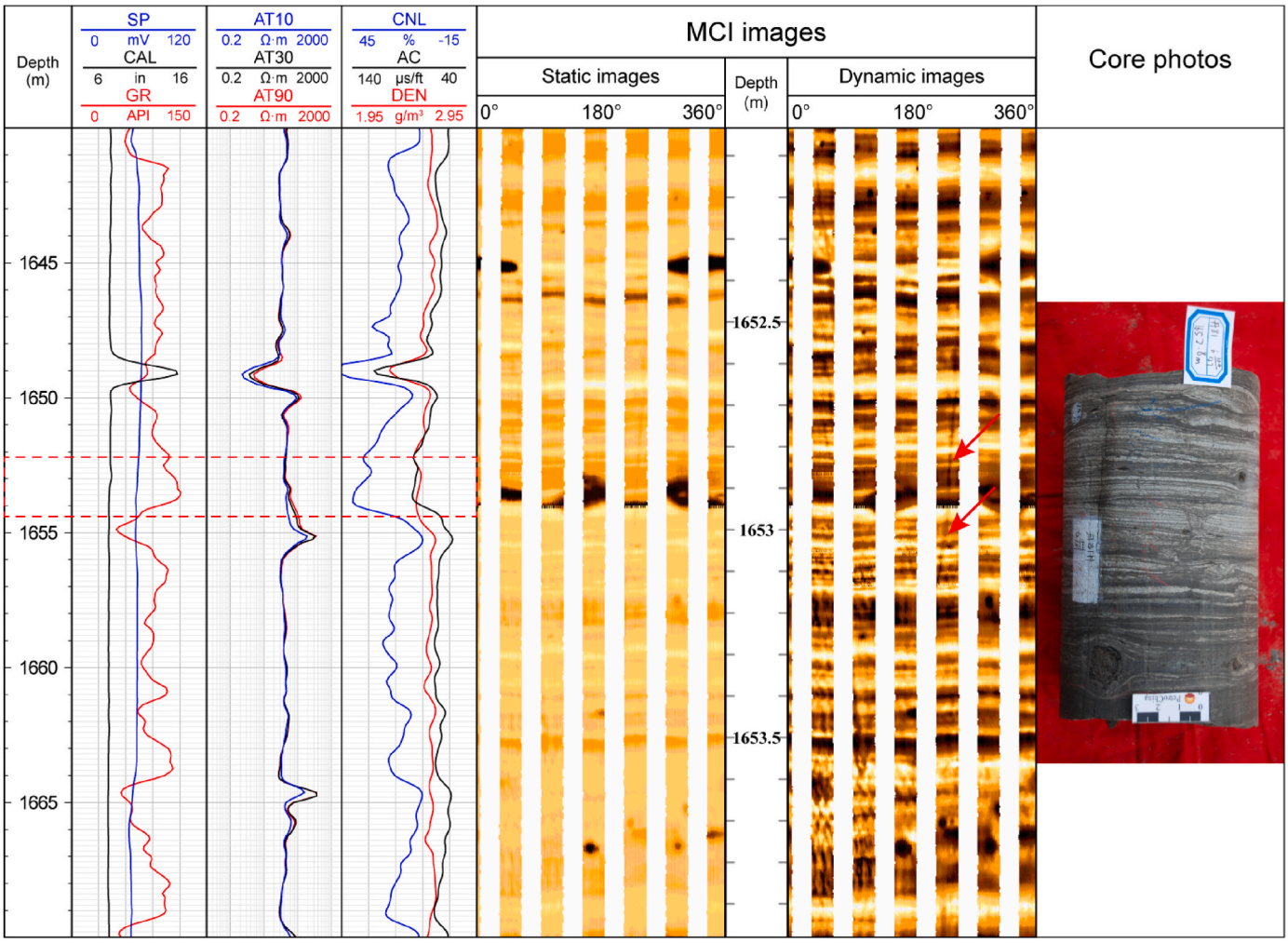

Fig. 6. Fracture identification template by image logs and conventional well logs under the core scale.

(Fig. 2b). Sonic Scanner log emits full-frequency scanning waves with high signal intensity, making it better suited for shear wave dispersion analysis than XMAC and DSI (Li et al., 2023b). Therefore, the radial slowness variations of fast and slow S-waves are used to reflect the anisotropy differences caused by natural fractures near wellbore in this study. The extension state and effectiveness of the fracture around the wellbore can be reflected by the intersection of the slowness difference of fast and slow S-waves in radial direction.

4. Results

4.1. Characteristics of fractures

Fractures can be divided into three types: tectonic fractures, diagenetic fractures, and abnormal high pressure fractures in the shale oil reservoirs according to genetic types (Gale et al., 2014). Tectonic fractures are the main fracture types in the study area. Tectonic fractures in the study area can be categorized into near-vertical (−90°) fractures, high-angle (75°–90°) fractures, and oblique (30°–75°) fractures according to the fracture occurrence (Lyu et al., 2022).

Vertical tectonic fractures, which are rarely filled with minerals, can be observed in the cores (Fig. 3a). Banded oil spots on the core show obvious oiliness. These fractures are clearly controlled by rock mechanics and typically terminate at the mudstone layer. High-angle and oblique shear fractures are predominantly found in fine sandstones and siltstones (Fig. 3b and c). The fracture surface of this kind of fracture is typically smooth and straight, generally not filled with calcite and other minerals. Low-angle shear fractures usually cut through the bedding interface of sandstones or shales and can be distinctly distinguished from faults in the core (Fig. 3d). Furthermore, multiple fractures filled with calcite are observed intersecting each other in the core, suggesting that the fractures in the study area have undergone multiple phases (Fig. 3e). Tectonic fractures are seldom detected in mudstone. Bedding-parallel fractures are diagenetic fractures that develop along the laminae planes of shale due to mechanical compaction and diagenesis (Fig. 3f and g). It is worth noting that not all lamina interfaces in shale can form bedding-parallel fractures. Only when the clay content at the bedding surface is moderate and the stress reaches the critical strength can it peel open and form fractures (Lai et al., 2022). Core observations show that these fractures primarily occur in the organic-rich shales of the Chang 7_3 interval and are often filled with calcite or other minerals. These fractures can serve as both dominant storage spaces in shale and critical seepage channels for shale oil (Fu et al., 2015; Guo et al., 2022).

In general, natural fracture and other matrix pore spaces together lead to the complex relationships between permeability and porosity in the study area (Fig. 4). Some data points of core samples in the low porosity region show high permeability, indicating the existence of natural fractures (Fig. 4).

4.2. Well log responses

4.2.1. Image log expressions of various geological objects

Well logs can provide stratigraphic and petrophysical information to recognize different geologic objects around wellbores (Lai et al., 2017;

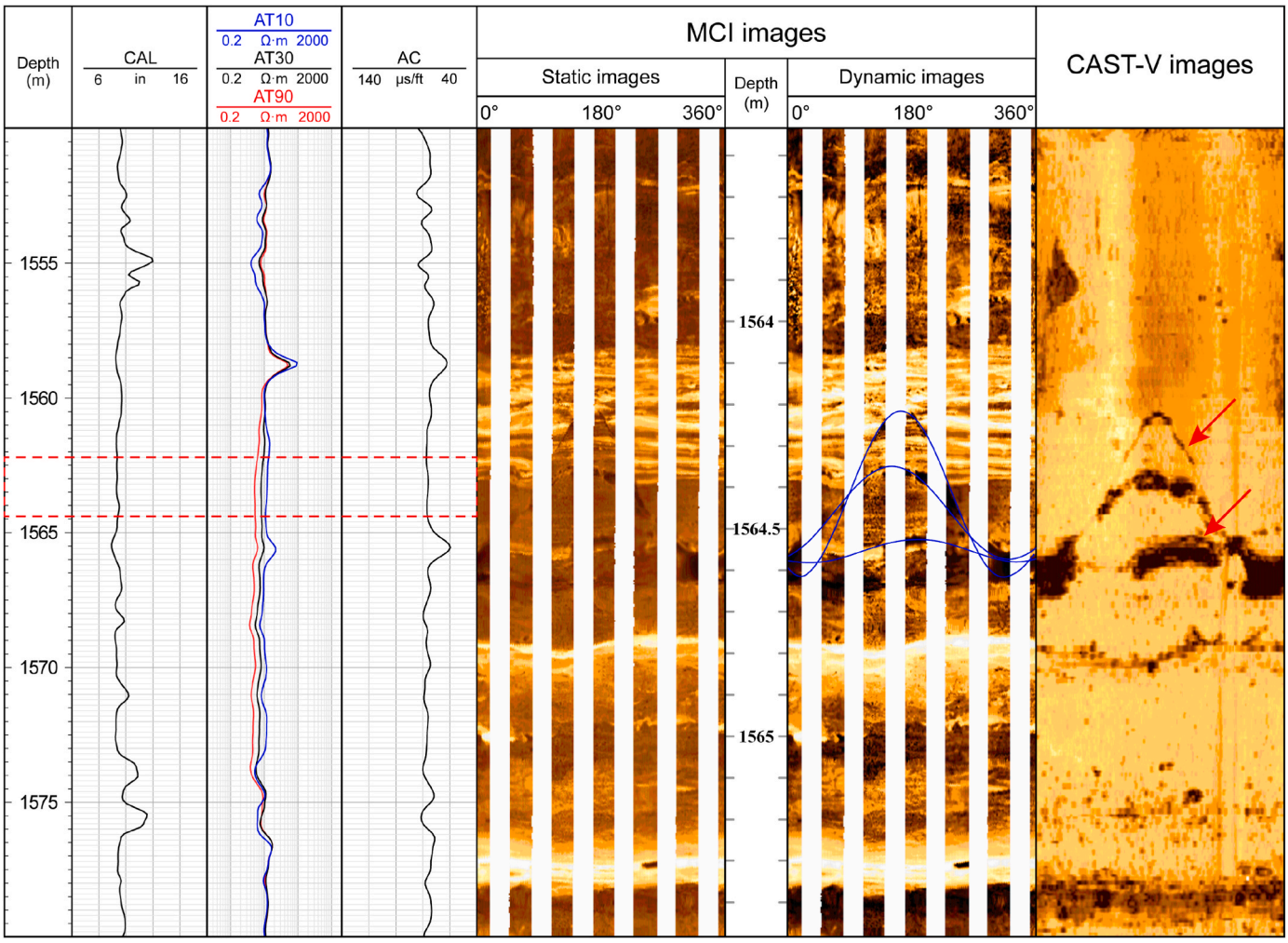

Fig. 7. Oblique open fractures identified by acoustic and electric image logs.

Aghli et al., 2020). Due to the limited vertical resolution of conventional well logs, it is difficult to accurately characterize fine-grained sedimentary rock reservoirs and shale reservoirs with strong heterogeneity (Zhang et al., 2021). In contrast, image logs have higher resolution (up to 0.2 inches) and provide clearer image data for recognition of geological objects (Nian et al., 2021). Therefore, the combination of conventional and image logs can effectively recognize and evaluate wellbore structures, such as fractures, bedding, micro-faults and borehole breakouts.

Natural fractures usually appear on image logs as continuous sinusoidal curves that cross the sedimentary stratigraphic plane of the formation (Fig. 5a). The amplitude and width of the sinusoidal curve are controlled by the natural fracture dip and forms. The color of the image logs reflects the conductivity difference of the rock around wellbore, which can reflect the filling of the fracture (Lai et al., 2024). In general, bright colors reflect high-resistance mineral fillings, while dark colors reflect low-resistance mineral fillings (Fig. 5b and c). For open fractures, the resistivity of the fracture is obviously lower than that of the surrounding rock due to the intrusion of water-based drilling fluid, showing low resistance dark sinusoidal lines (Fig. 5d).

Bedding-parallel fractures are formed by the breakage of mechanically weak laminae planes, usually parallel to the laminae surface in shale (Pang et al., 2023). Due to the stress from overburden formation, bedding-parallel fracture apertures are generally very small, unless the fluid migration and dissolution occur along bedding interfaces (Lai et al., 2022). Bedding-parallel fractures partially filled by calcite or pyrite often appear as discontinuous sinusoidal curves on image logs (Fig. 5e). In addition, it is possible to distinguish well between bedding-parallel fractures and argillaceous strips by the difference in thickness and conductivity of the sinusoidal curves on image logs.

Faults are common geological structures in the study area. Similar to natural fractures, faults also appear as continuous sinusoidal curves on image logs. They are clearly recognized by the dislocation of the bedding and the variation of the inclination of the surrounding strata (Fig. 5f). The fault strikes are closely related to the tectonic evolution of the study area and changes in the in-situ stress fields.

Induced fractures are usually formed by human factors such as in-situ stress relief and readjustment in the process of drilling and fracturing (Brudy and Zoback, 1999). These fractures typically manifest as two vertical or geometrically en-echelon fractures oriented 180° apart on image logs (Fig. 5g and h). The difference between induced fractures and natural fractures on image logs is that induced fractures exhibits no continuous sinusoidal curves (Ju et al., 2020). In other words, the curve of induced fractures has no peaks or troughs. Induced fracture strikes are parallel to the orientation of in-situ SH_{max} (maximum horizontal stress).

Borehole breakouts refer to the enlargement of the wellbore, which usually occurs in pure mudstone intervals (Wilson et al., 2015). It is usually caused by the formation pressure exceeds the compressive strength of the wellbore rock or the drilling fluid density is too small to support the wellbore. Breakouts appears as parallel dark bands 180° apart on image logs (Fig. 5i). The orientation of the borehole breakouts is 90° different from induced fracture strikes, indicating the orientation of the in-situ Sh_{min} (minimum horizontal stress) (Nian et al., 2016).

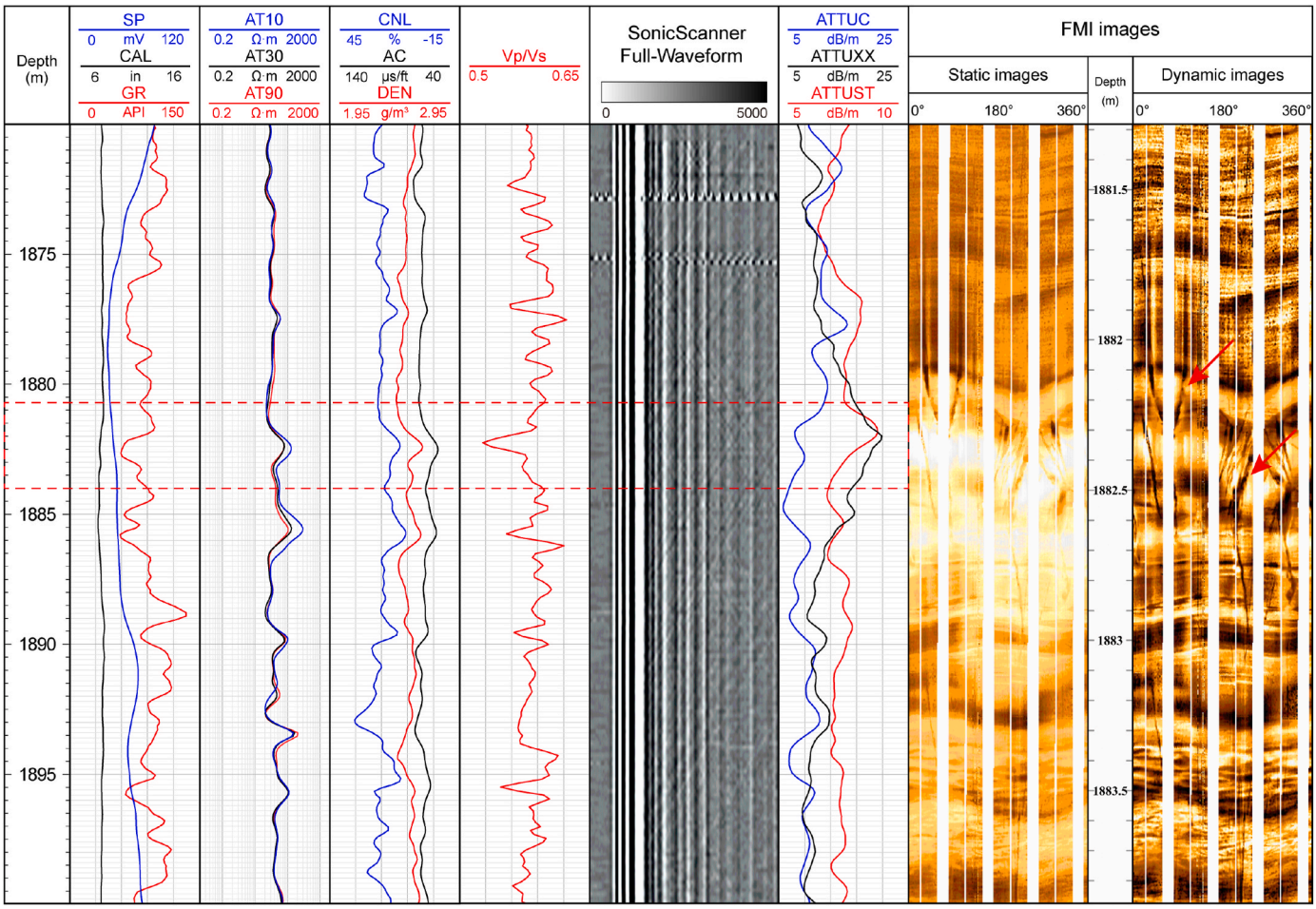

Fig. 8. Natural fractures around the borehole predicted by the Vp/Vs ratio, energy attenuation, waveform distortion of array acoustic logs. ATTUC: P-wave energy attenuation curve, ATTUXX: S-wave energy attenuation curve, ATTUST: St-wave energy attenuation curve.

4.2.2. *Recognition of fractures using acoustic and electric image logs*

The wells in the study area were drilled using water-based mud drilling fluids, including various types of electric image log such as FMI, XRMI, and MCI. Since oil-based mud drilling fluids were not employed, the results of fracture detection will not be compromised by a decrease in the resolution of the image logs. When the core data from the drilled wells are comprehensive and complete, an absolute match between core data and image log data is achieved through the precise core homing (Canady et al., 2008; Nian et al., 2021). The depth of the core corresponds to the depth of the log to a uniform depth by means of the calcareous nodules on the core and the response characteristics on image logs. Thus, a link between distinct geological objects and image logs can be established (Pang et al., 2023). Near-vertical fractures are controlled by the rock mechanical layers and usually do not extend more than 1m. This type of fracture shows no distinct response characteristics on conventional logging curves. Instead, it manifests as a dark, continuous curve on image logs (Fig. 6). The reliability of image logs is enhanced by establishing the fracture recognition templates under the core scale.

However, it is difficult to accurately detect natural fractures through electric image logs alone when there is less core data or low resolution due to abnormal measurement of image logs (Wang et al., 2022). Full borehole images with high accuracy from acoustic image logs can compensate for the low coverage of electric image logs and reduce the uncertainty of fracture interpretation. It can be seen that the sinusoidal curves of the fractures are not obvious on the MCI image logs. While three open fractures can be clearly detected on the CAST-V acoustic image logs, all fractures show dark continuous sinusoidal curves with dissolution (Fig. 7). Particularly in the context of oil-based mud drilling fluids, acoustic image logs have advantages over electric image logs for fracture detection (Momeni et al., 2019). Acoustic image logs can meet the needs of different environments such as open hole and cased hole wells (Dewhurst et al., 2011). However, due to the fact that acoustic image logs need to be measured in the hole center, the quality of the image is seriously affected by well inclination and borehole. Therefore, fractures can be recognized by a combination of acoustic and electric image logs in complex borehole environments.

4.2.3. *Recognition of fractures using array acoustic logs*

The fundamental principle of array acoustic logs is to measure the acoustic properties of formation by transmitting and receiving sonic waves. The propagation speed and attenuation characteristics of these waves in the formation are affected by the petrophysical properties, such as lithology, porosity and fractures. The presence of natural fractures in rocks leads to changes in the propagation characteristics of compressional wave (P-wave), shear wave (S-wave) and Stoneley wave (St-wave) in the formation (Pickett, 1963). Therefore, acoustic velocity variations, energy attenuation and waveform distortions from array acoustic logs can be utilized to recognize and predict fractures around the borehole (Tang et al., 2007, 2011; Lai et al., 2017).

When there are vertical fractures or high-angle fractures in the rocks, the formation exhibits characteristics similar to the Horizontal Transverse Isotropy (HTI). In this case, S-wave slowness propagating along the vertical direction increases significantly, but P-wave slowness is less affected. So high-angle fractures will lead to a relative decrease in the ratio of P- and S-wave slowness (Vp/Vs). While there are low-angle fractures and bedding-parallel fractures in the rocks, and the

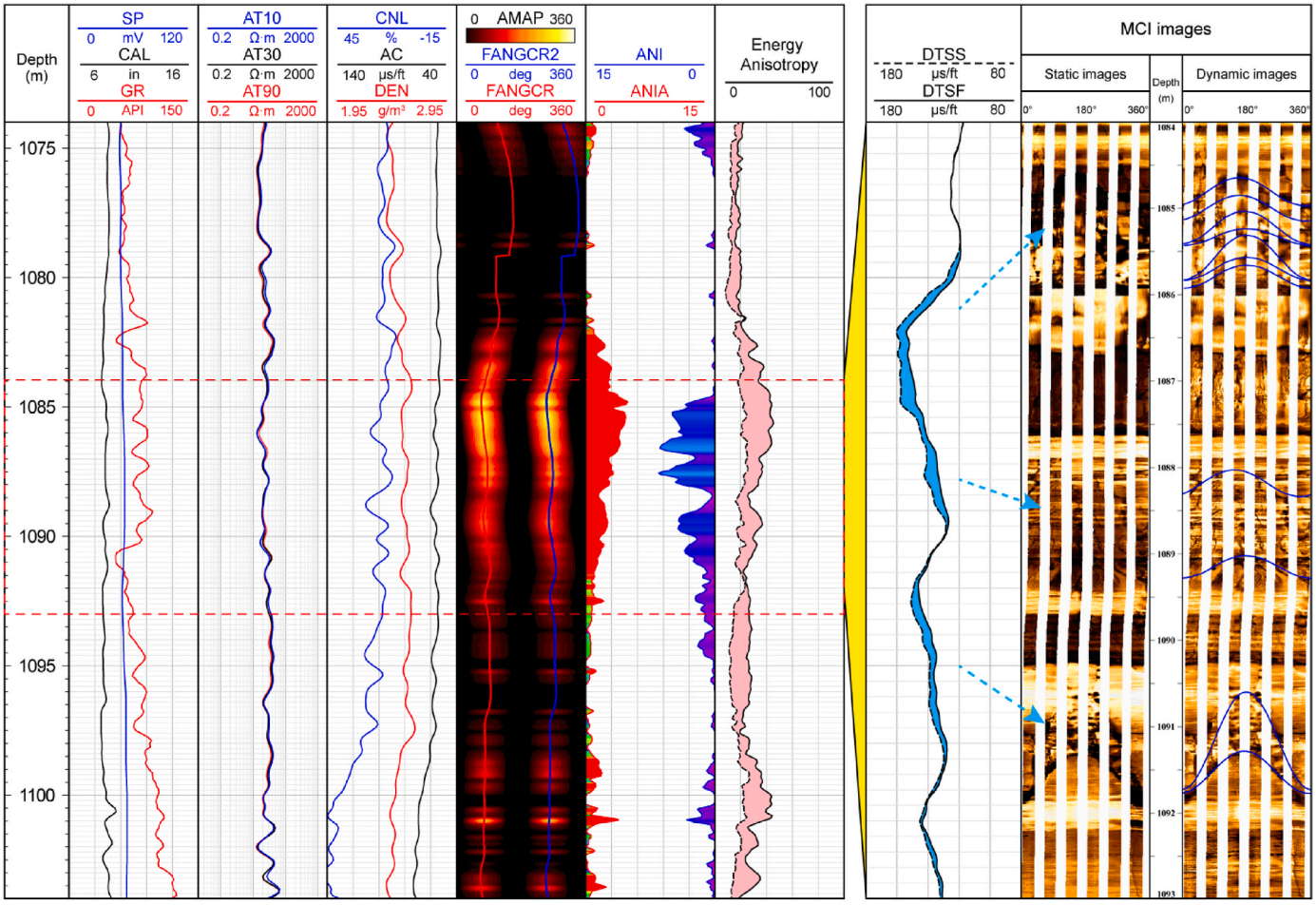

Fig. 9. Natural fractures evaluated by the magnitude of S-wave slowness anisotropy determined from dipole acoustic logs. ANI: S-wave slowness anisotropy curve, ANIA: S-wave slowness array anisotropy curve, DTSS: Slow S-wave slowness curve, DTSF: Fast S-wave slowness curve.

formation exhibits characteristics similar to the Vertical Transverse Isotropy (VTI). P- and S-wave slowness is difficult to reflect the difference between these fractures and the sedimentary bedding surfaces. In addition, borehole enlargement and lithology changes also cause the change of Vp/Vs ratios. It is necessary to combine other information to eliminate this multiplicity.

The attenuation characteristics of acoustic waves can be used to predict the inclination and effectiveness of natural fractures (Hornby et al., 1989; Lee et al., 2019). Low-angle fractures and bedding-parallel fractures cause changes in wave impedance in the longitudinal direction of the formation, which results in attenuation of the traveling P-wave energy amplitude. Acoustic wave attenuation reflects low-angle fractures only if the borehole is perpendicular to the formation. And high-angle fractures cause changes in the wave impedance in the transverse direction of the formation, which results in attenuation of the traveling S-wave energy amplitude. Open fractures provide channels for fluid migration and improve the permeability of the formation. St-waves propagating along the borehole sidewall are reflected at these fracture sites, leading to energy loss and attenuation. After obtaining direct, upward and downward reflected waves through various filtering methods, the St-wave reflection coefficients can be calculated to quantitatively estimate fracture apertures (Tang et al., 2011). In other words, the strength of the reflected St-wave energy can predict fracture apertures and opening status. St-wave attenuation increases with the increasing fracture degree. From approximately 1880 m–1885 m depth in the Chang 6 shale oil reservoirs of well Gu23, the Vp/Vs ratio decreases sharply (Fig. 8). The energy attenuation coefficients of S-wave and St-wave increase obviously, while the compressional wave shows little change, possibly indicating the presence of high-angle open fractures. Many fractures can be observed on the FMI image logs. And the presences of these fractures could also be evidenced by significant “V” shaped reflection stripes of Sonic Scanner full-waveforms (Fig. 8). The “V” reflection stripe of mode wave energy attenuation in the full-waveforms of array acoustic logs can qualitatively explain the fracture section. The strength of the interference fringes can qualitatively reflect fracture opening status, but cannot distinguish the sedimentary bedding planes from the low-angle fractures.

S-wave splitting is the principle of evaluating fractures by using formation anisotropy (Tang et al., 2011). In fractured formations, the incident S-waves will split into two groups parallel and perpendicular to the fracture trend. The velocity of S-waves parallel to the fracture strike is faster than that perpendicular to the fracture strike, which is called azimuth anisotropy. S-waves parallel to the fracture strike are called fast S-waves, while others are called slow S-waves. S-wave slowness anisotropy will increase with the increasing fracture degree (Prioul et al., 2007). Thus, fracture zones can be evaluated by the magnitude of S-wave slowness anisotropy determined from dipole acoustic logs (Tang et al., 2016; Li et al., 2022). Fig. 9 shows the response characteristics on the XMAC array acoustic logs of Chang 7 shale oil reservoir in well Dan228. The depth of 1085–1090 m shows strong S-wave slowness anisotropy and energy anisotropy. There are also some differences in values between the slowness curves of fast and slow S-wave. It is noteworthy that the three fracture intervals on the MCI image logs correspond to these differences (Fig. 9). The combination of the image logs and array acoustic logs indicates that these intervals are highly fractured. However, not all types of fractures can be detected by anisotropy.

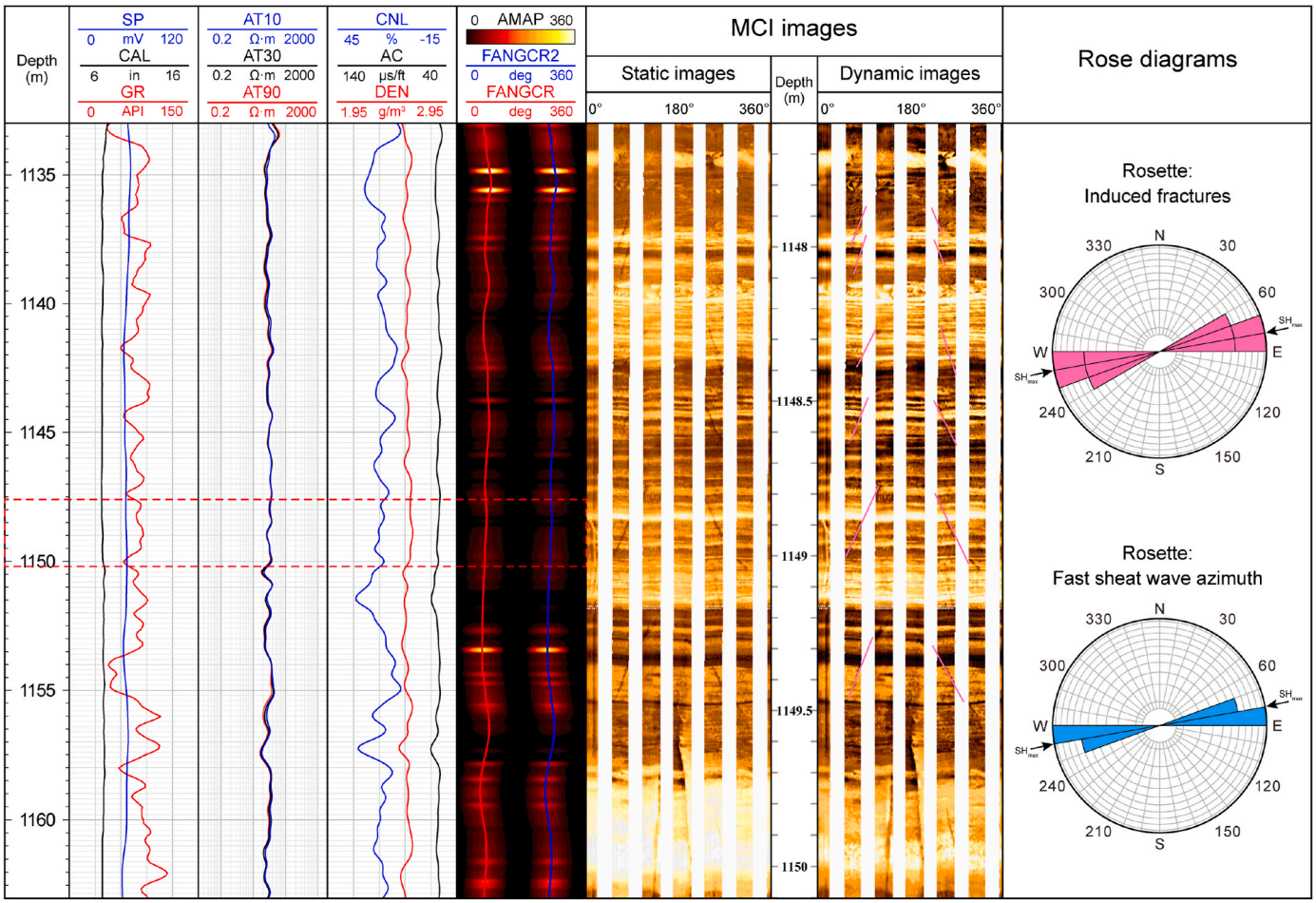

Fig. 10. Determination of the present in-situ SHmax direction using induced fracture strike and fast S-wave azimuth.

The anisotropy of fractures filled with mud or calcite tends to be weak and difficult to detect. Non-fracture factors such as in-situ stress, formation dip, and elliptical boreholes can also lead to large S-wave slowness anisotropy.

5. Discussion

5.1. Fracture distribution within in-situ stress fields

Natural fractures are common in formation rocks, which is the result of the comprehensive influence of geological structure, mechanical in-situ stress field and fluid action. In-situ stress fields play a significant role in controlling the formation, distribution and characteristics of natural fractures (Bell and Gough, 1979; Ju et al., 2020). Therefore, clarifying the mechanism and relationship between in-situ stress and fractures is important for drilling engineering and hydrocarbon production.

5.1.1. Fracture and in-situ stress direction

The 3D distribution of the in-situ stress field determines the stress state in the rock. The direction of SH_{max} is often the direction where fractures are most easily opened. Variations in the in-situ stress field are the main reason for the multiple stages of fractures (Brudy and Zoback, 1999). In addition, the type of natural fractures is also related to the in-situ stress field. For example, shear fractures are more common in the area dominated by shear stress. The paleotectonic in-situ stress field controls the fracture extension orientation, while the present in-situ stress field controls the fracture openness and connectivity (Baouche et al., 2023; Lai et al., 2023). Therefore, the research on present in-situ stress is very important for predicting and evaluating the effectiveness of fractures (Kingdon et al., 2016).

The present in-situ stress direction can be determined using the characteristics of rock fractures caused by stress on image logs (Ju et al., 2020). During the drilling process, due to the coupling effect between the stress concentration and mud pressure, induced fractures or borehole breakouts are formed under specific borehole conditions. Induced fractures are mainly caused by the release of structural stress in the stress-concentrated formation due to drilling tools. This results in their orientation being parallel to the direction of the in-situ SH_{max}. The orientation of the borehole breakouts is 90° different from induced fracture strikes, indicating the orientation of the in-situ Sh_{min} (minimum horizontal stress) (Nian et al., 2016). The polarization direction of the fast S-wave indicates the direction of the in-situ SH_{max} (Wang et al., 2022). The XMAC anisotropy analysis results show that the direction of S-waves is located at about 70–80° (Figs. 10 and 11). It is observed that the SH_{max} direction given by image logs aligns with the fast S-wave direction. However, there are limitations in determining the present in-situ stress direction from fast S-wave orientations. The dominant direction of S-wave slowness anisotropy is controlled by in-situ stress fields only when the effects of natural fractures and formation dip are excluded (Wang et al., 2022). And S-wave slowness anisotropy is not suitable for predicting the in-situ stress direction in the interval with low stress difference ($\Delta\sigma = SH_{max} - Sh_{min}$). Thus, image logs and array acoustic logs each have their respective advantages in analyzing in-situ stress direction and need to be combined to ensure the accuracy of interpretation.

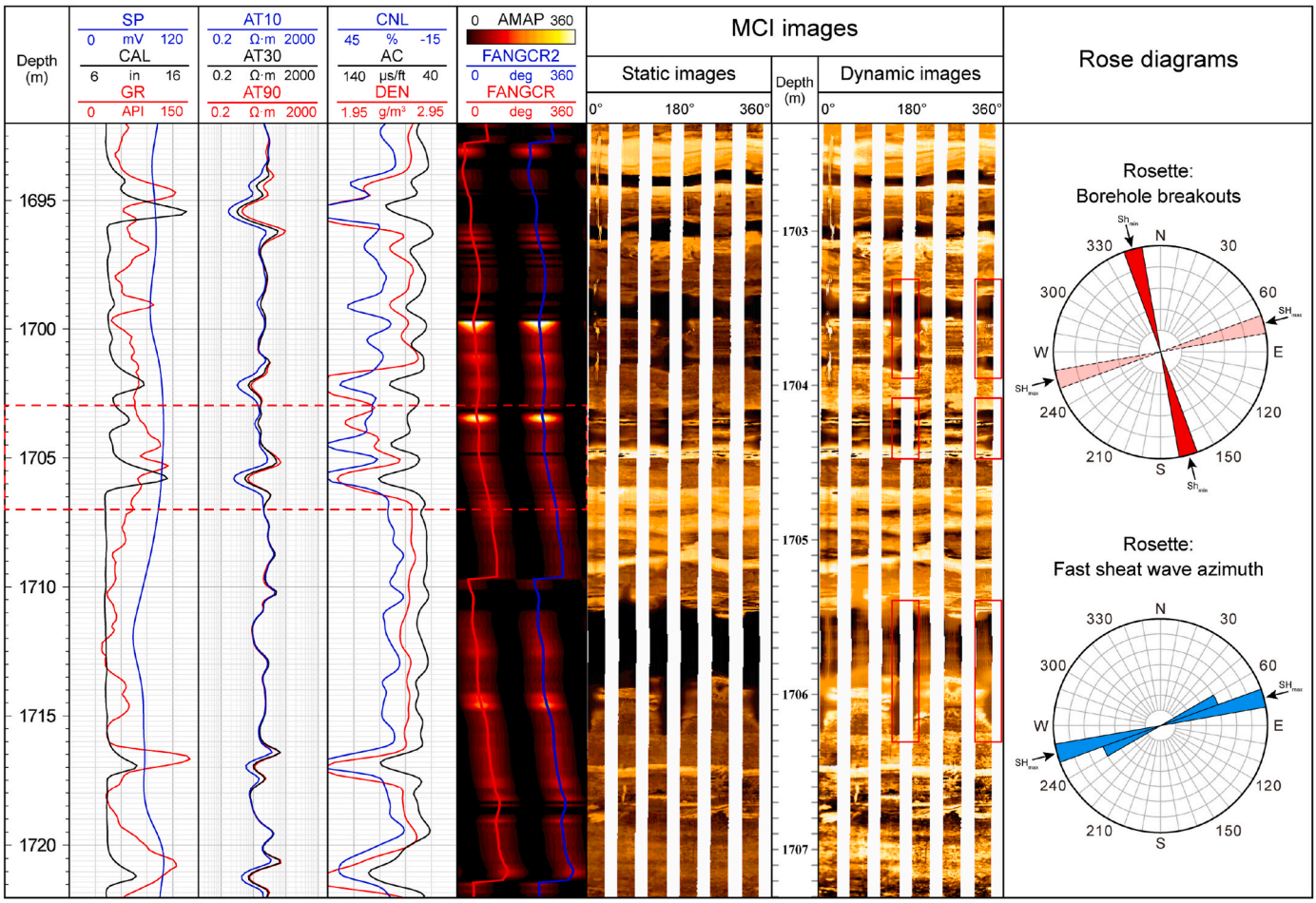

Fig. 11. Determination of the present in-situ SHmax direction using borehole breakout orientation and fast S-wave azimuth.

5.1.2. Distribution of fractures in a single well

Figs. 12 and 13 show the image logs interpretation results of fractures and other geological objects in the Chang 6 to Chang 8 intervals of two wells in the study area. The green lines, blue lines, yellow lines, pink lines and red lines represent bedding planes, conductive fractures, resistive fractures, induced fractures and borehole breakouts, respectively. The two dominant orientations of the bedding planes are both ENE–WSW, indicating relatively minor variation in dip throughout the Chang 6 to Chang 8 intervals in well Gao57. Resistive fracture strikes in the same direction as the bedding planes in well Gao 57, both showing two groups in the ENE-WSW direction (Fig. 12). In contrast, the dominant strike of the resistive fractures well Gu 23 well is consistent with micro-faults (Fig. 13). The strike of conductive fractures and induced fractures in both wells is dominated by ENE-WSW. It is worth noting that there are few natural fractures and a large number of faults are detected by image logs in well Gu23 (Fig. 13).

Vertically, the types and distributions of natural fractures vary among different stratigraphic intervals. In the Chang 6 interval, oblique and low-angle fractures predominate, with roughly equal numbers of unfilled and filled fractures. Numerous high-angle and oblique fractures are detected in the upper part of the Chang 7 interval, most of which are open fractures, while there are more micro-faults of Well Gu 23. In the Chang 7_3 interval, a large number of low-angle fractures and bedding-plane fractures are detected in the high-GR shale with abundant bedding planes. Oblique fractures and low-angle fractures dominate in Chang 8 interval, while some micro-faults are still visible in this section of well Gu 23.

The variation in fracture inclination between the two wells appears closely tied to the spatial extent of micro-fault development. The strikes of the micro-faults align with resistive fractures. Induced fractures exhibit ENE-WSW strikes, indicating the orientation of in-situ SHmax (Fig. 13). In other words, the micro-fault strikes are almost parallel to the orientation of the in-situ Shmin. This results in considerable variation in bedding plane orientation due to the presence of micro-faults. The angle between the micro-fault strikes and the direction of the current in-situ Shmin is small (20°), suggesting minimal accumulation of fault stress. The direction of the tectonic stress field has not experienced significant changes, and the current in-situ stress shows strong inheritance (Ju et al., 2020). Overall, the strikes of high-angle open fractures detected on image logs are parallel to the in-situ SHmax direction or within 30° of the intersection angles, indicating large fracture apertures and good connectivity.

5.2. Impact of fractures on reservoir quality

5.2.1. Fracture parameters

Previous studies have shown that natural fractures have multiple effects on shale reservoir quality (Ding et al., 2012; Xu et al., 2020). The existence of natural fractures can not only connect isolated pore spaces, but also serve as good storage spaces in shale, thereby jointly improving the effective porosity of the reservoir. More importantly, natural fractures can be used as hydrocarbon micro-migration channels to improve the reservoir seepage properties (Anders et al., 2014; Du et al., 2023a,b). The pore and permeability analysis above also shows that the permeability of the fractured sample was significantly higher than that of the non-fractured interval sample (Fig. 4).

The impact of natural fractures on reservoir quality is directly controlled by a range of fracture parameters such as fracture porosity,

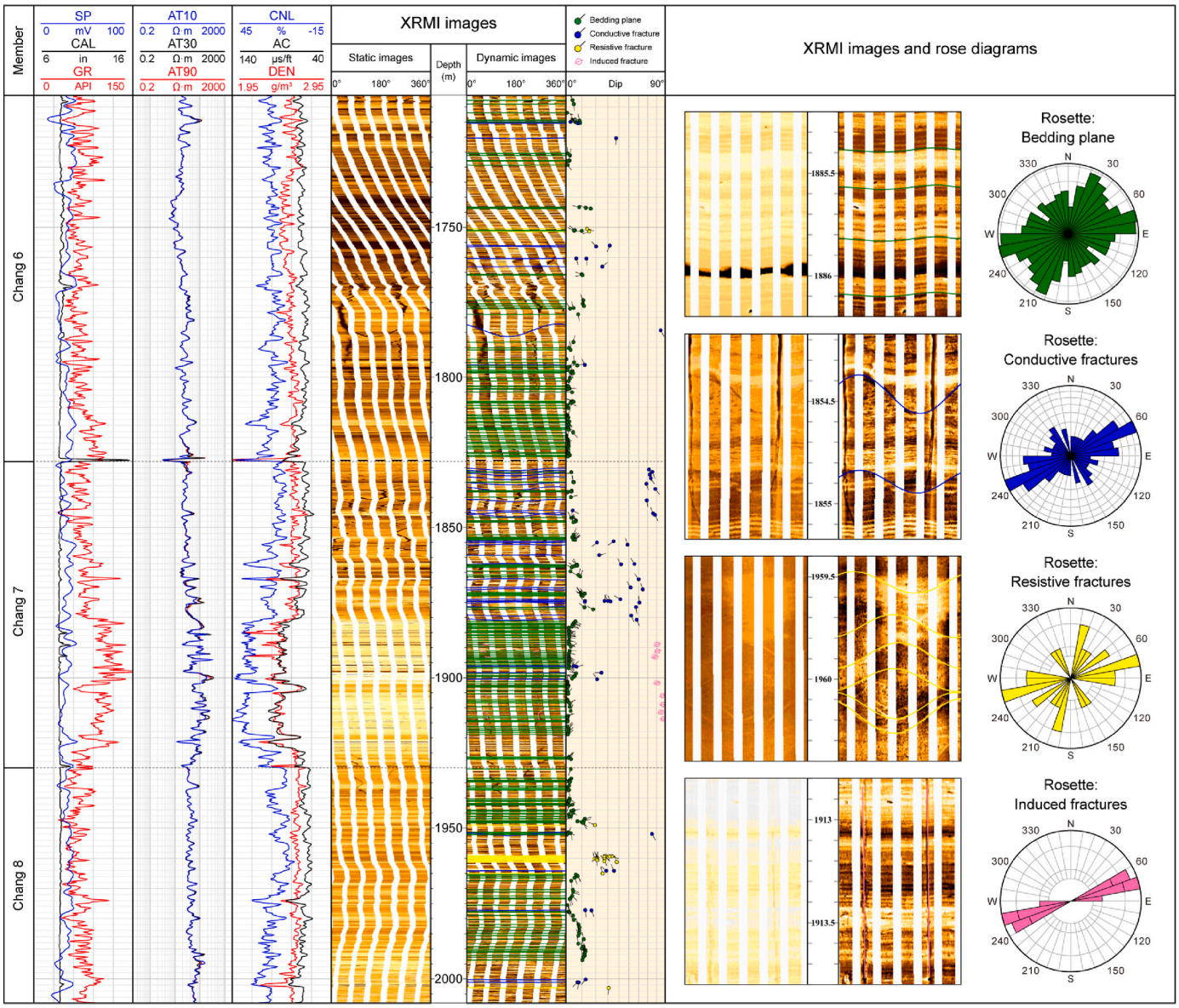

Fig. 12. Comprehensive evaluation of conductive fractures, resistive fractures, induced fractures, borehole breakouts, and bedding planes using image logs (Gao57).

permeability, aperture and filling degree of fractures (Marghani et al., 2023). In addition to direct core observation and experiments, evaluating natural fracture parameters usually requires the integration of multiple methods such as log interpretation and productivity analysis (Xu et al., 2018; Lai et al., 2024). Image logs can not only directly recognize fracture occurrence (strike, dip direction, dip angle), but also further process and calculate fracture density (FVDC), fracture aperture (FAVH), fracture porosity (FVPA) and other fracture parameters under the condition of water-based drilling fluids (Lai et al., 2017; Aghli et al., 2020). Fig. 14 shows the results of fracture detection and calculation parameters in the Chang 6 to Chang 7 intervals of well Gu23 using image logs. The depth of 1925–1940 m shows no natural fractures on image logs and tight siltstone is visible on core observations. The pore distribution plot shows a single peak with left deviation, and the left column representing the small pores is large (Fig. 14a). The depth of 1985–2000 m shows many oblique conductive fractures, resistive fractures and micro-faults are detected on image logs. There are 8 resistive fractures and 5 conductive fractures. Fracture parameter calculations show that the total natural fracture density in this interval averages 2.42 m-1, peaking at 5 m-1. The average open fracture aperture is 0.12 mm, and the maximum open fracture porosity can reach up to 0.02%. The calculated fracture parameters also indicate a good effectiveness of open fractures. It can be seen that the siltstone and mudstone bands are vertically overlapped, and low-angle fractures are existed in the siltstone bands. The pore distribution plot visually reflects the characteristics of the existence of natural fractures. There is bimodal peak and the column area representing large pores on the right is significantly increased (Fig. 14b).

Fracture parameters are also influenced by diagenetic sequence. The effectiveness of fractures could be decreased by cementation in the early diagenetic stage. These fractures are likely to be filled by minerals such as calcite to be invalid fractures. However, dissolution often creates pores along fractures and improves fracture effectiveness (Figs. 7 and 9). The stronger the later dissolution, the better the fracture effectiveness. And considerable acidic water brought by hydrocarbon injection could dissolve fracture surfaces and cements, further improving fracture porosity and permeability. Therefore, dissolution is regarded as a constructive diagenesis improving fracture effectiveness and reservoir quality significantly.

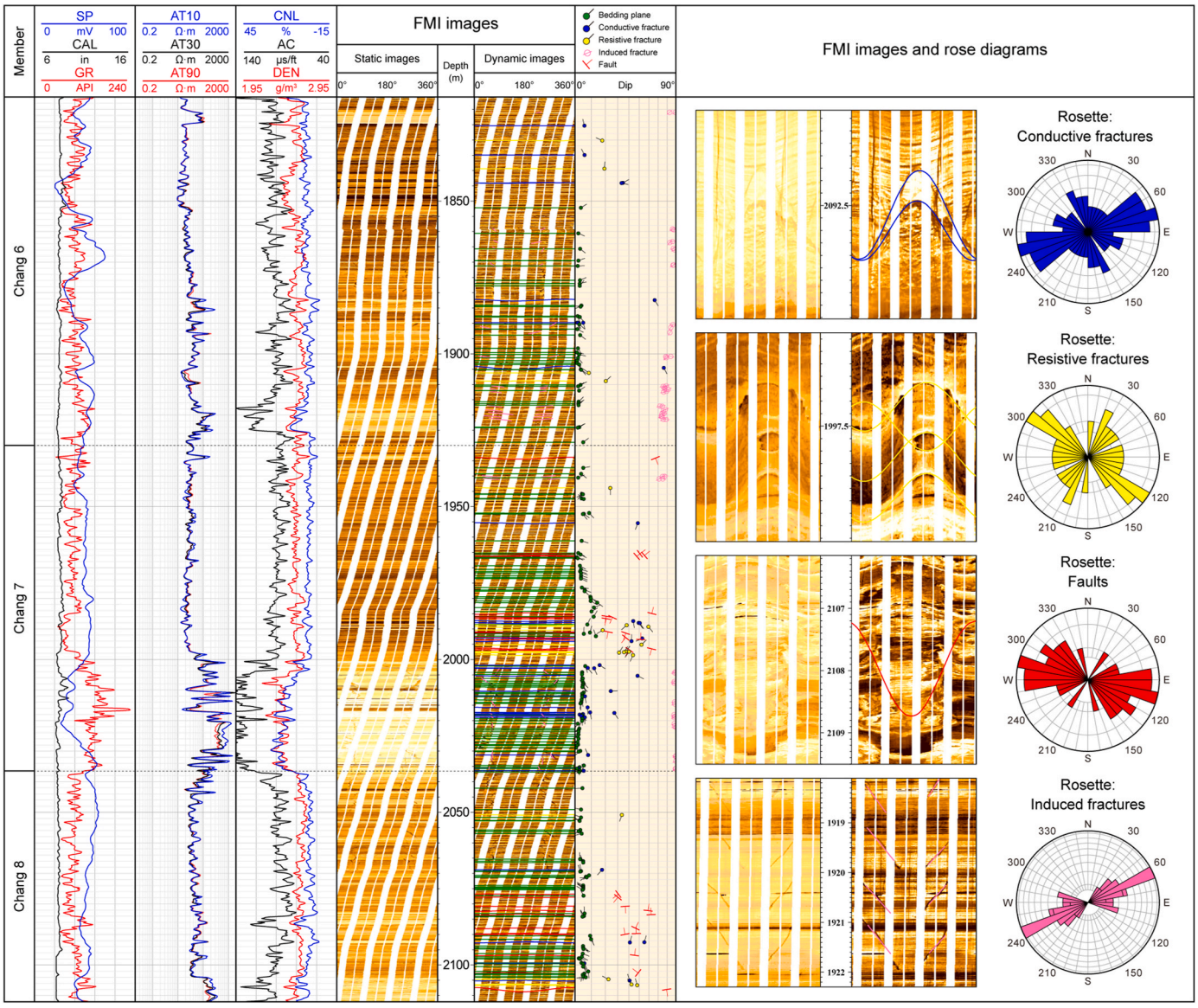

Fig. 13. Comprehensive evaluation of conductive fractures, resistive fractures, microfaults, induced fractures, and bedding planes using image logs (Gu23).

5.2.2. Fracture radial extension

The intersection and extension of fracture assemblage types with different occurrences directly determine the distribution of fracture network in shale reservoirs (Zou et al., 2016). A highly connected open fracture network can ensure thus guarantee the seepage property and migration efficiency of fluids (Zeng et al., 2023). The mechanical stability of fractures affects their ability to maintain an open state. Stable natural fractures can remain open during the production process and help maintain efficient fluid flow over time. In contrast, completely filled fractures will lose the seepage channel and be regarded as ineffective fractures (Nian et al., 2021). On the other hand, shale oil reservoir usually has many vertical production layers, with the "sweet spot" body exhibiting obvious thin interbed characteristics. It is crucial to fully utilize the vertical production layer. Horizontal well volumetric fracturing is an effective means to develop shale oil efficiently (Zhao et al., 2024). The coupling relationship between natural fractures and hydraulic fractures in hydraulic fracturing is determined by the extension state of natural fractures around the borehole (Yang et al., 2022). The existence of natural fractures can communicate the vertical heterogeneous layers and realize the effective fracturing of multilayer systems (Zhang et al., 2023). This controls the extension height of artificial fractures and the complexity of the fracture network, which affects the volumetric fracturing effect of shale oil (Fu et al., 2015). In summary, characterization of the occurrence properties and extension state of natural fractures in borehole and near borehole is essential for evaluating fracture effectiveness.

Limited by core observation scale and seismic ant attribute map detection accuracy, well logs are considered to be the most effective means to recognize and predict fractures (Tang et al., 2011; Lai et al., 2017; Boersma et al., 2020). Different logging instruments have different radial detection depths. As previously mentioned, the vast majority of natural fractures around the borehole can be recognized using a combination of image and array acoustic logs (Fig. 8). Remote detection acoustic image logs use acoustic reflection wave pre-stacking migration imaging to recognize reflectors up to 50m around the borehole, including fractures and faults (Liu et al., 2023). However, not all wells measure remote detection acoustic image logs. Therefore, the radial slowness variations of fast and slow S-waves are used to reflect the anisotropy differences caused by natural fractures near wellbore in this study (Tang et al., 2016). Fractures across the borehole can be detected using image logs and S-wave slowness anisotropy (Fig. 9). The extension state of the fracture around wellbore can be reflected by the intersection

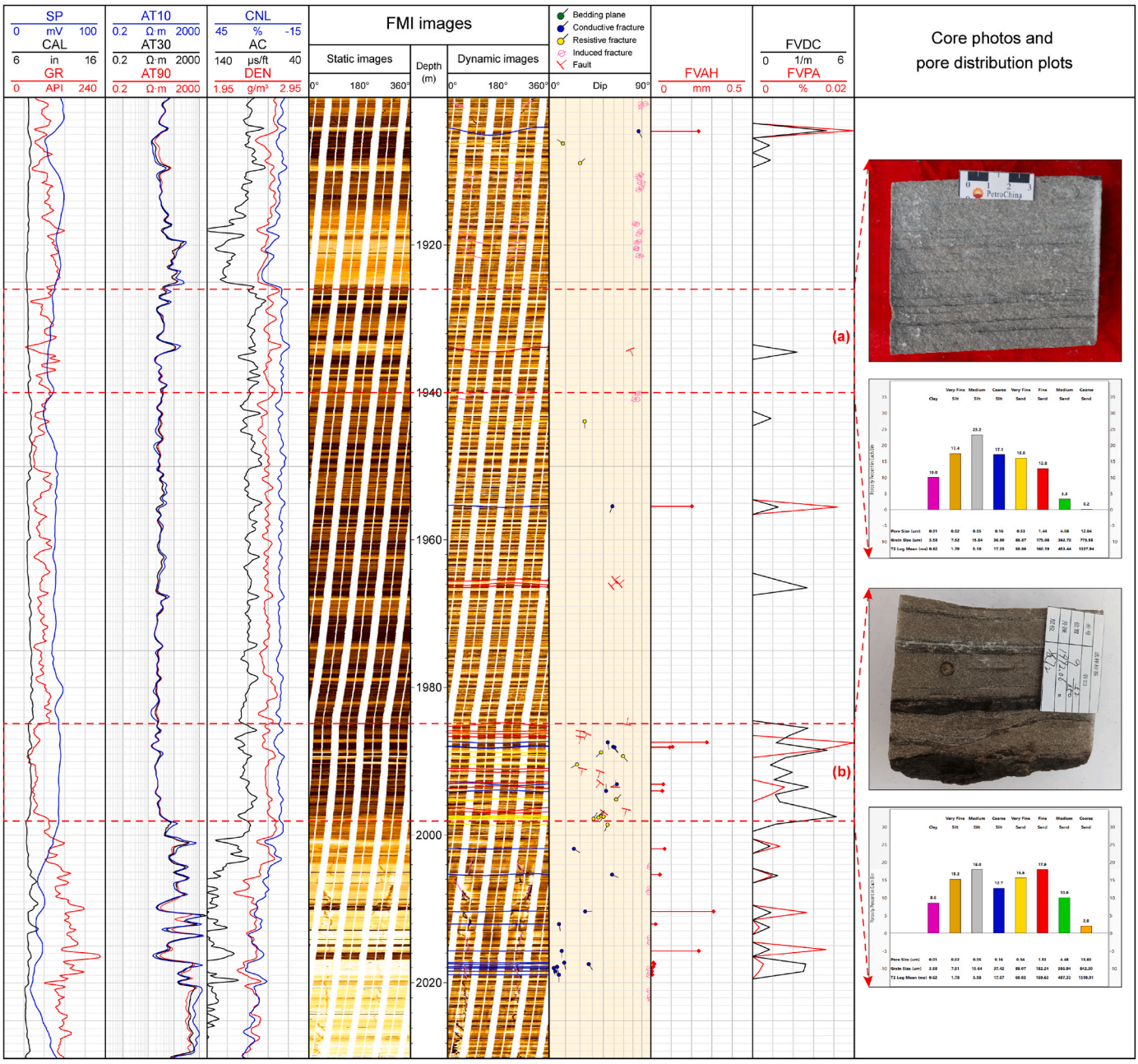

Fig. 14. Fracture parameters such as fracture density (FVDC), fracture aperture (FAVH), fracture porosity (FVPA) provided by image logs. (a). Non-fracture intervals show tight siltstone on core observation. (b). Intervals with natural fractures and microfaults show many large pores in the pore distribution plot.

of the slowness difference of fast and slow S-waves in radial direction (Li et al., 2023b). Fig. 15 illustrates the response characteristics of fracture assemblage type intervals with different occurrences on image logs, array acoustic logs, and 2D NMR logs. Fig. 15a shows a non-fracture interval with many bedding planes. There is no separation of fast and slow S-waves in radial propagation, and the differences in values between the slowness curves of fast and slow S-wave is small. On the contrary, with the increase of radial propagation distance, the fast and slow S-waves will separate and cross. Fig. 15b shows an interval with oblique conductive fractures, and the slowness curve of fast and slow S-wave waves in radial propagation appears a cross. While the slowness curve of fast and slow S-wave waves in radial propagation of the interval with low-angle fractures and bedding-parallel fractures cross twice (Fig. 15c). Therefore, a combination of fracture occurrence and type detected by image logs, along with the fracture extension state indicated by fast and slow S-wave radial variations, can accurately evaluate fracture effectiveness around wellbores (Tang et al., 2011, 2016; Li et al., 2022).

In addition, The T_1-T_2 map from 2D NMR logs can also be used to illustrate the impact of fractures on reservoir quality (Fleury and Romero-Sarmiento, 2016; Huang et al., 2023). The lower left energy cluster signifies bound fluids such as bound water and bitumen within the pores, while the upper right energy cluster represents free fluids such as movable oil and movable water in the pores (Wang et al., 2021) (Fig. 15). It is evident that the upper right high-energy cluster in the T_1-T_2 maps of the fracture intervals is larger than that of the non-fracture intervals (Fig. 15a and b). This indicates a substantial amount of movable oil in the pores, reflecting better reservoir quality. Due to the high organic matter and clay mineral content in the Chang 7_3 interval, the section with low-angle fractures and bedding-parallel fractures exhibits numerous clay-bound water signals (Fig. 15c).

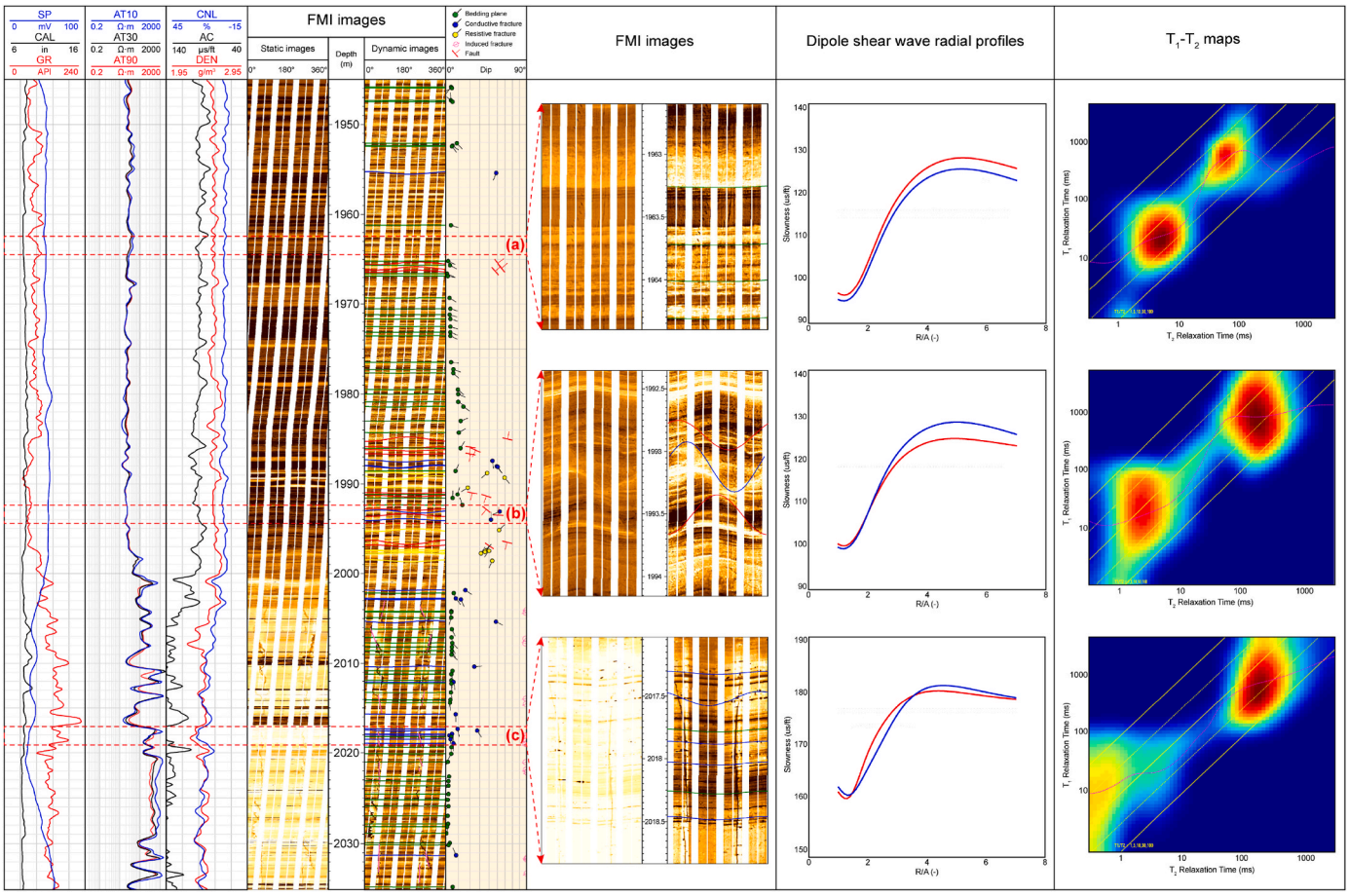

Fig. 15. The response characteristics of fracture assemblage type intervals with different occurrences on image logs, array acoustic logs, and 2D NMR logs.

5.2.3. *Relationship between fracture and in-situ stress*

The inherent properties of natural fractures mentioned above primarily influence the fracture effectiveness. The relationship between fracture and in-situ stress is a crucial external factor impacting hydrocarbon productivity (Gong et al., 2021; Xu et al., 2022). Generally, the formation of tectonic fractures is controlled by the paleotectonic in-situ stress fields, while the fracture aperture and permeability are influenced by the present in-situ stress fields. The intervals with low horizontal present in-situ stress difference ($\Delta\sigma = SH_{max}$ - Sh_{min}) usually correspond to high fracture aperture and porosity (Lai et al., 2023). Natural fractures that are nearly parallel to the direction of the in-situ SH_{max} are regarded as effective fractures, exhibiting tensile properties with good connectivity and permeability (Nian et al., 2021). In contrast, natural fractures that are approximately vertical to the direction of the in-situ SH_{max} are in an extruded state and are deemed invalid fractures. Fig. 16 illustrates the results of the natural fracture effectiveness evaluation of the Chang 7_3 shale oil reservoirs in well Gu21. The depth of 1998–2006 m shows multiple high-angle open fractures detected by image logs. And the presences of these fractures could also be evidenced by significant "V" shaped reflection stripes and strong S-wave slowness anisotropy. The dominant natural fracture orientations are 40°–100° and 220°–280°, which are parallel to the in-situ SH_{max} direction or within 30° of the intersection angles. These natural fractures, which appear as dark sinusoidal waves on image logs, have large apertures and good connectivity. The presences of fractures enhance the hydrocarbon productivity significantly (a daily oil production of 6.12 m^3).

The relationship between fracture and in-situ stress can also guide the drilling orientation and hydraulic fracturing of horizontal wells (Liu et al., 2023). Artificial fractures easily expand along the in-situ SH_{max} direction during hydraulic fracturing. To achieve a large fracture network and reservoir reconstruction volume, horizontal wells are typically drilled along the in-situ Sh_{min} direction or at an angle of less than 30° (Xu et al., 2022). Consequently, natural fractures and horizontal present in-situ stress difference together control the morphology and distribution of artificial fracture network during reservoir reconstruction (Zou et al., 2016; Zhang et al., 2023). The smaller the horizontal present in-situ stress difference, the more complex the fracture network becomes. The coupling relationship between natural fractures and hydraulic fractures governs the complexity of the artificial fracture network formed during hydraulic fracturing (Li et al., 2022; Yang et al., 2022). However, if the natural fracture density in the overlap zone of water injection development is too high or interconnected with production wells, there may be a risk of pressure channeling or leakage, leading to lower recovery. Therefore, accurately recognizing and clarifying the contribution of natural fractures to reservoir quality is essential for improving the development effectiveness of shale reservoirs.

6. Conclusion

Natural fractures can be effectively detected by integrating various logging techniques (electric image and array acoustic logs) with core observations. Acoustic velocity variation, energy attenuation and waveform distortion from array acoustic logs can be used to recognize and predict fractures around the borehole. The extension state of the fracture around the wellbore is reflected by fast and slow S-wave radial variations. Combining the occurrence and type of fractures detected by image logs and the fracture extension state indicated by fast and slow shear wave radial variations, the effectiveness of fractures around the wellbore can be accurately evaluated. Integrating fracture parameters with shear wave anisotropy analysis reveals how effective fractures

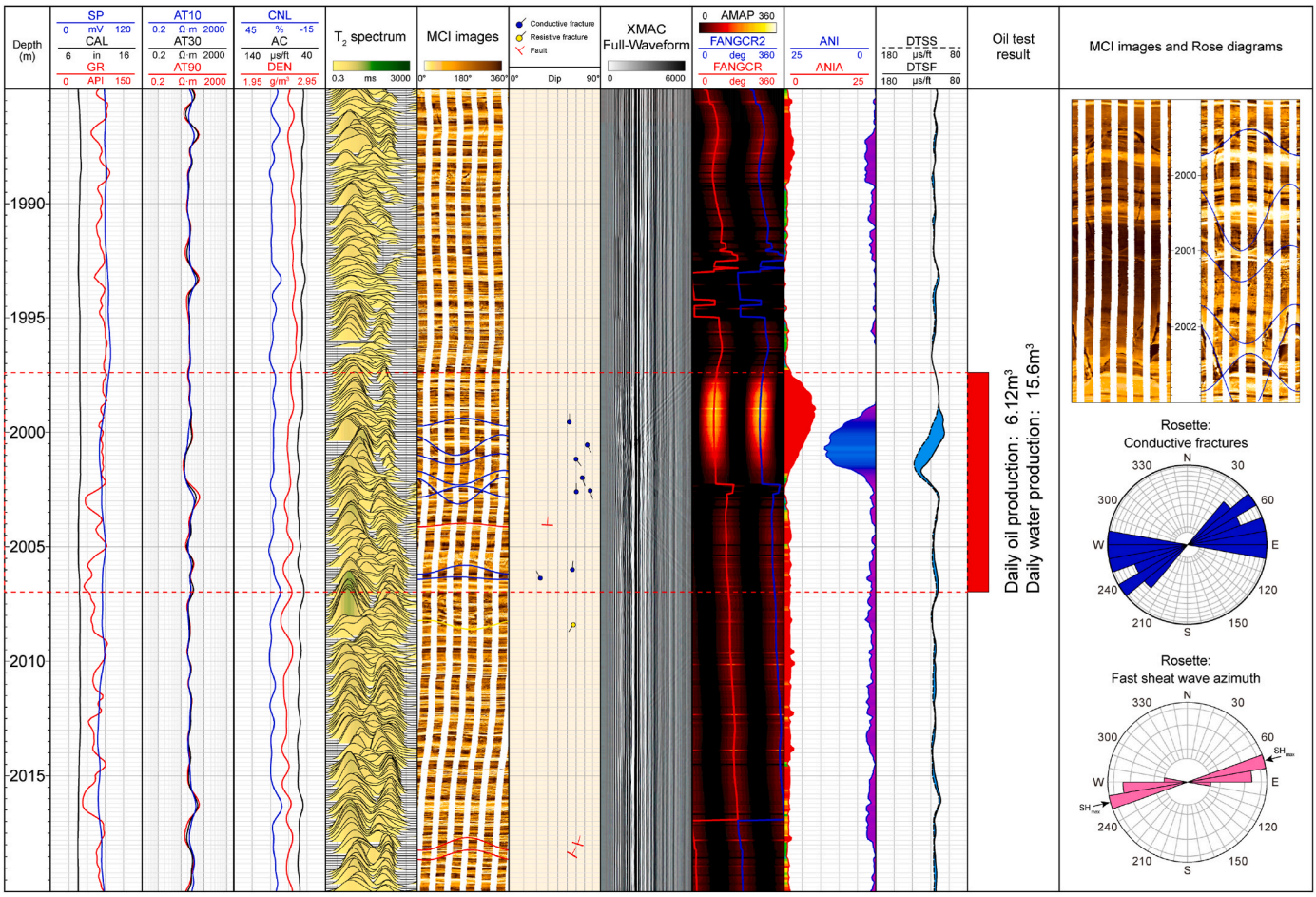

Fig. 16. Natural fracture effectiveness evaluation and their controls on hydrocarbon productivity of the Chang 7_3 shale oil reservoirs in well Gu21.

within the in-situ stress field impact reservoir quality. High-angle open fractures that are parallel to or within 30° of the in-situ SH_{max} direction typically exhibit better flow capacity and connectivity, making them critical pathways for improving shale oil production. The research above may aid in optimizing sweet spot evaluation and stimulating shale oil production.

CRediT authorship contribution statement

Yuyue Huang: Writing – review & editing, Writing – original draft, Investigation. **Guiwen Wang:** Resources, Project administration, Funding acquisition. **Lichun Kuang:** Resources, Project administration, Funding acquisition. **Chaoliu Li:** Software, Methodology. **Ming Wang:** Software, Methodology. **Song Wang:** Visualization, Investigation. **Hongbin Li:** Visualization, Investigation. **Fei Zhao:** Visualization, Investigation. **Jin Lai:** Writing – review & editing, Methodology.

Declaration of competing interest

The authors declare that they have no known competing financial interests or personal relationships that could have appeared to influence the work reported in this paper.

Acknowledgments

This work is financially supported by the National Natural Science Foundation of China (Grant No. 41872133 and No. 42002133). Thanks to the editors for their enthusiasm, patience, and tireless efforts. The authors thank the reviewers for their constructive suggestions on how to improve the paper.

Data availability

Data will be made available on request.

References

Aghli, G., Moussavi-Harami, R., Mohammadian, R., 2020. Reservoir heterogeneity and fracture parameter determination using electrical image logs and petrophysical data (a case study, carbonate Asmari Formation, Zagros Basin, SW Iran). Petrol. Sci. 17 (1), 51–69.

Anders, M.H., Laubach, S.E., Scholz, C.H., 2014. Microfractures: a review. J. Struct. Geol. 69, 377–394.

Baouche, R., Sen, S., Radwan, A.E., Abd El Aal, A., 2023. In situ stress determination based on acoustic image logs and borehole measurements in the in-adaoui and bourarhat hydrocarbon fields, eastern Algeria. Energies 16 (10), 4079.

Bell, J.S., Gough, D.I., 1979. Northeast-southwest compressive stress in Alberta: evidence from oil wells. Earth Planet Sci. Lett. 45 (2), 475–482.

Boersma, Q., Athmer, W., Haege, M., Etchebes, M., Haukås, J., Bertotti, G., 2020. Natural fault and fracture network characterization for the southern Ekofisk field: a case study integrating seismic attribute analysis with image log interpretation. J. Struct. Geol. 141, 104197.

Brudy, M., Zoback, M.D., 1999. Drilling-induced tensile wall-fractures; implications for determination of in-situ stress orientation and magnitude. Int. J. Rock Mech. Min. Sci. Geomech. Abstracts 36 (2), 191–215.

Canady, W., Market, J., Anonymous, 2008. Fracture characterization by borehole logging methods. Petrophysics 49 (2), 206.

Chandra, D., Vishal, V., 2021. A critical review on pore to continuum scale imaging techniques for enhanced shale gas recovery. Earth Sci. Rev. 217, 103638.

Curtis, J.B., 2002. Fractured shale-gas systems. AAPG (Am. Assoc. Pet. Geol.) Bull. 86 (11), 1921–1938.

Dewhurst, D.N., Siggins, A.F., Sarout, J., Raven, M.D., Nordgård-Bolås, H.M., 2011. Geomechanical and ultrasonic characterization of a Norwegian Sea shale. Geophysics 76 (3), WA101–WA111.

Ding, W., Li, C., Li, C., Xu, C., Jiu, K., Zeng, W., Wu, L., 2012. Fracture development in shale and its relationship to gas accumulation. Geosci. Front. 3 (1), 97–105.
Dong, S., Zeng, L., Wang, L., Lyu, W., Xu, H., Ji, C., Zhang, F., Xu, W., 2024. Fracture identification in shale reservoir using a deep learning method: Chang 7 reservoirs, Triassic Yanchang formation. Geoenergy Science and Engineering 238, 212853.
Donselaar, M.E., Schmidt, J.M., 2005. Integration of outcrop and borehole image logs for high-resolution facies interpretation; example from a fluvial fan in the Ebro Basin, Spain. Sedimentology 52 (5), 1021–1042.
Du, X., Jin, Z., Zeng, L., Liu, G., He, W., Ostadhassan, M., Song, Y., Liang, X., Yang, S., Lu, G., 2023a. Formation of natural fractures and their impact on shale oil accumulation in the Mahu Sag, Junggar Basin, NW China. Int. J. Coal Geol. 279, 104385.
Du, X., Jin, Z., Zeng, L., Liu, G., He, W., Ostadhassan, M., Liang, X., Yang, S., Lu, G., 2023b. Characteristics and controlling factors of natural fractures in deep lacustrine shale oil reservoirs of the Permian Fengcheng Formation in the Mahu Sag, Junggar Basin, China. J. Struct. Geol. 175, 104923.
Fleury, M., Romero-Sarmiento, M., 2016. Characterization of shales using T1-T2 NMR maps. J. Petrol. Sci. Eng. 137, 55–62.
Fu, H., Wang, X., Zhang, L., Gao, R., Li, Z., Zhu, X., Xu, W., Li, Q., Xu, T., 2015. Geological controls on artificial fracture networks in continental shale and its fracability evaluation: a case study in the Yanchang Formation, Ordos Basin, China. J. Nat. Gas Sci. Eng. 26, 1285–1293.
Fu, J., Li, S., Niu, X., Deng, X., Zhou, X., 2020. Geological characteristics and exploration of shale oil in Chang 7 member of triassic Yanchang Formation, Ordos Basin, NW China. Petrol. Explor. Dev. 47 (5), 931–945.
Gale, J.F.W., Laubach, S.E., Olson, J.E., Eichhubl, P., Fall, A., 2014. Natural fractures in shale; a review and new observations. AAPG (Am. Assoc. Pet. Geol.) Bull. 98 (11), 2165–2216.
Gale, J.F.W., Reed, R.M., Holder, J., 2007. Natural fractures in the Barnett Shale and their importance for hydraulic fracture treatments. AAPG (Am. Assoc. Pet. Geol.) Bull. 91 (4), 603–622.
Gong, L., Wang, J., Gao, S., Fu, X., Liu, B., Miao, F., Zhou, X., Meng, Q., 2021. Characterization, controlling factors and evolution of fracture effectiveness in shale oil reservoirs. J. Petrol. Sci. Eng. 203, 108655.
Gou, Q., Xu, S., Hao, F., Yang, F., Zhang, B., Shu, Z., Zhang, A., Wang, Y., Lu, Y., Cheng, X., Qing, J., Gao, M., 2019. Full-scale pores and micro-fractures characterization using FE-SEM, gas adsorption, nano-CT and micro-CT: a case study of the Silurian Longmaxi Formation shale in the Fuling area, Sichuan Basin, China. Fuel 253, 167–179.
Guo, Q., Li, S., Jin, Z., Zhou, X., Liu, C., 2023. Characteristics and exploration targets of Chang 7 shale oil in triassic Yanchang Formation, Ordos Basin, NW China. Petrol. Explor. Dev. 50 (4), 878–893.
Guo, Q., Yao, Y., Hou, L., Tang, S., Pan, S., Yang, F., 2022. Oil migration, retention, and differential accumulation in “sandwiched” lacustrine shale oil systems from the Chang 7 member of the Upper Triassic Yanchang Formation, Ordos Basin, China. Int. J. Coal Geol. 261, 104077.
Haldorsen, J.B.U., Johson, D.L., Plona, T., et al., 2006. Borehole acoustic waves. Schlumberger Oilfield Review 18 (1), 34–43.
He, D., 2022. Multi-cycle superimposed sedimentary basins in China: formation, evolution, geologic framework and hydrocarbon occurrence. Earth Sci. Front. 29 (6), 24–59.
Hooker, J.N., Cartwright, J., Stephenson, B., Silver, C.R.P., Dickson, A.J., Hsieh, Y., 2017. Fluid evolution in fracturing black shales, Appalachian Basin. AAPG (Am. Assoc. Pet. Geol.) Bull. 101 (8), 1203–1238.
Hornby, B.E., Johnson, D.L., Winkler, K.W., et al., 1989. Fracture evaluation using reflected Stoneley-wave arrivals. Geophysics 54 (10), 1274–1288.
Huang, Y., Wang, G., Zhang, Y., Xi, J., Huang, L., Wang, S., Zhang, Y., Lai, J., Jiang, C., 2023. Logging evaluation of pore structure and reservoir quality in shale oil reservoir: the Fengcheng Formation in Mahu Sag, Junggar Basin. China. Mar. Petrol. Geol. 156, 106454.
Hughes, J.D., 2013. Energy: a reality check on the shale revolution. Nature 494 (7437), 307–308.
Jarvie, D.M., 2012. Shale resource systems for oil and gas: Part 2dshale oil resource systems. In: Breyer, J.A. (Ed.), Shale ReservoirsdGiant Resources for the 21st Century, vol. 97. AAPG (Am. Assoc. Pet. Geol.) Bull, pp. 89–119.
Jiang, M., Jin, Y., Fu, X., Wang, H., Meng, L., 2023. The development of cataclastic bands in high-porosity sandstones: insights from ring shear experiments. J. Struct. Geol. 175, 104952.
Jiang, M., Fu, X., Wang, Z., 2024. An experimental investigation of the characteristics of cataclastic bands in high-porosity sandstones. Geol. Soc. Am. Bull. 136 (7–8), 3069–3084.
Ju, W., Niu, X., Feng, S., You, Y., Xu, K., Wang, G., Xu, H., 2020. Predicting the present-day in situ stress distribution within the Yanchang Formation Chang 7 shale oil reservoir of Ordos Basin, central China. Petrol. Sci. 17 (4), 912–924.
Kingdon, A., Fellgett, M.W., Williams, J.D.O., 2016. Use of borehole imaging to improve understanding of the in-situ stress orientation of Central and Northern England and its implications for unconventional hydrocarbon resources. Mar. Petrol. Geol. 73, 1–20.
Kuang, L., Hou, L., Wu, S., Cui, J., Tian, H., Zhang, L., Zhao, Z., Luo, X., Jiang, X., 2022. Organic matter occurrence and pore-forming mechanisms in lacustrine shales in China. Petrol. Sci. 19 (4), 1460–1472.
Lai, J., Chen, K., Xin, Y., Wu, X., Chen, X., Yang, K., Song, Q., Wang, G., Ding, X., 2021. Fracture characterization and detection in the deep Cambrian dolostones in the Tarim Basin, China: insights from borehole image and sonic logs. J. Petrol. Sci. Eng. 196, 107659.
Lai, J., Liu, B., Li, H., Pang, X., Liu, S., Bao, M., Wang, G., 2022. Bedding parallel fractures in fine-grained sedimentary rocks: recognition, formation mechanisms, and prediction using well log. Petrol. Sci. 19 (2), 554–569.
Lai, J., Wang, G., Fan, Z., Wang, Z., Chen, J., Zhou, Z., Wang, S., Xiao, C., 2017. Fracture detection in oil-based drilling mud using a combination of borehole image and sonic logs. Mar. Petrol. Geol. 84, 195–214.
Lai, J., Zhao, F., Zhang, M., Bai, T., Huang, Y., Li, D., Wang, G., Qin, Z., 2023. How high can fracture porosity become in the ultra-deep subsurface? Geosci. Front. 14 (5), 101617.
Lai, J., Su, Y., Xiao, L., Zhao, F., Bai, T., Li, Y., Li, H., Huang, Y., Wang, G., Qin, Z., 2024. Application of geophysical well logs in solving geologic issues: past, present and future prospect. Geosci. Front. 15 (3), 101779.
Lee, S., Li, H., Gu, X., Tang, X., 2019. Near-borehole characteristics of hydraulic fractures and fracturing-induced sonic-wave attenuation. Geophysics 84 (3), D81–D87.
Li, H., Tang, X., Li, S., Su, Y., 2022. Dynamic fluid transport property of hydraulic fractures and its evaluation using acoustic logging. Petrol. Explor. Dev. 49 (1), 223–232.
Li, H., Wang, G., Li, Y., Bai, M., Pang, X., Zhang, W., Zhang, X., Wang, Q., Ma, X., Lai, J., 2023a. Fault-Karst systems in the deep ordovician carbonate reservoirs in the yingshan Formation of tahe oilfield tarim basin, China. Geoenergy Science and Engineering 231, 212338.
Li, J., He, X., Zhao, A., et al., 2023b. Joint inversion of formation radial shear-velocity profiles by dipole acoustic logging while drilling. Geophysics 88 (4), D295–D305.
Liu, B., Sun, J., Zhang, Y., et al., 2021. Reservoir space and enrichment model of shale oil in the first member of Cretaceous Qingshankou Formation in the Changling sag, southern Songliao Basin, NE China. Petrol. Explor. Dev. 48 (3), 1–16.
Liu, P., Li, N., Wu, H., et al., 2023. Fracture characterization in shale and tight reservoirs using horizontal well sonic logging data. Third International Meeting for Applied Geoscience & Energy. Society of Exploration Geophysicists and American Association of Petroleum Geologists, pp. 1760–1764.
Liu, Q., Chen, M., Liu, W., Li, J., Han, P., Guo, Y., 2009. Origin of natural gas from the Ordovician paleo-weathering crust and gas-filling model in Jingbian gas field, Ordos Basin, China. J. Asian Earth Sci. 35 (1), 74–88.
Loucks, R.G., Reed, R.M., Ruppel, S.C., Hammes, U., 2012. Spectrum of pore types and networks in mudrocks and a descriptive classification for matrix-related mudrock pores. AAPG Bull. 96 (6), 1071–1098.
Lyu, W., Zeng, L., Liu, Z., Liu, G., Zu, K., 2016. Fracture responses of conventional logs in tight-oil sandstones: a case study of the Upper Triassic Yanchang Formation in southwest Ordos Basin, China. AAPG Bull. 100 (9), 1399–1417.
Lyu, W., Zeng, L., Lyu, P., Yi, T., Dong, S., Wang, S., Xu, X., Chen, H., 2022. Insights into the mechanical stratigraphy and vertical fracture patterns in tight oil sandstones: the Upper Triassic Yanchang Formation in the eastern Ordos Basin, China. J. Petrol. Sci. Eng. 212, 110247.
Lyu, W., Zeng, L., Zhou, S., Du, X., Xia, D., Liu, G., Li, J., Weng, J., 2019. Natural fractures in tight-oil sandstones: a case study of the upper triassic Yanchang Formation in the southwestern Ordos Basin, China. AAPG Bull. 103 (10), 2343–2367.
Marghani, M.M.A., Zairi, M., Radwan, A.E., 2023. Facies analysis, diagenesis, and petrophysical controls on the reservoir quality of the low porosity fluvial sandstone of the Nubian formation, east Sirt Basin, Libya: insights into the role of fractures in fluid migration, fluid flow, and enhancing the permeability of low porous reservoirs. Mar. Petrol. Geol. 147, 105986.
Momeni, A., Rostami, S., Hashemi, S., Mosalman-Nejad, H., Ahmadi, A., 2019. Fracture and fluid flow paths analysis of an offshore carbonate reservoir using oil-based mud images and petrophysical logs. Mar. Petrol. Geol. 109, 349–360.
Nian, T., Wang, G., Tan, C., Fei, L., He, W., Wang, S., 2021. Hydraulic apertures of barren fractures in tight-gas sandstones at depth: image-core calibration in the lower cretaceous Bashijiqike Formation, Tarim Basin. J. Petrol. Sci. Eng. 196, 108016.
Nian, T., Wang, G., Xiao, C., Zhou, L., Deng, L., Li, R., 2016. The in situ stress determination from borehole image logs in the Kuqa Depression. J. Nat. Gas Sci. Eng. 34, 1077–1084.
Pang, X., Wang, G., Kuang, L., Zhao, F., Li, C., Wang, C., Zhang, M., Lai, J., 2023. Lamellation fractures in shale oil reservoirs: recognition, prediction and their influence on oil enrichment. Mar. Petrol. Geol. 148, 106032.
Pickett, G.R., 1963. Acoustic character logs and their applications in formation evaluation. Journal of Petroleum technology 15 (6), 659–667.
Prioul, R., Donald, A., Koepsell, R., et al., 2007. Forward modeling of fracture-induced sonic anisotropy using a combination of borehole image and sonic logs. Geophysics 72 (4), E135–E147.
Strijker, G., Bertotti, G., Luthi, S.M., 2012. Multi-scale fracture network analysis from an outcrop analogue: a case study from the Cambro-Ordovician clastic succession in Petra, Jordan. Mar. Petrol. Geol. 38 (1), 104–116.
Tang, X., Bolshakov, A., Patterson, D., 2011. Integrated acoustic evaluation of reservoir fractures: from borehole out into the formation. Petrophysics 52 (3), 199–206.
Tang, X., Xu, S., Zhuang, C., Su, Y., Chen, X., 2016. Quantitative evaluation of rock brittleness and fracability based on elastic-wave velocity variation around borehole. Petrol. Explor. Dev. 43 (3), 457–464.
Tang, X., Zheng, Y., Patterson, D., 2007. Processing array acoustic-logging data to image near-borehole geologic structures. Geophysics 72 (2), E87–E97.
Tian, Y., Wang, G., Li, H., Huang, Y., Zhao, F., Guo, Y., Gao, J., Lai, J., 2024. A novel deep learning method based on 2-D CNNs and GRUs for permeability prediction of tight sandstone. Geoenergy Science and Engineering 238, 212851.
Wang, S., Wang, G., Huang, L., Song, L., Zhang, Y., Li, D., Huang, Y., 2021. Logging evaluation of lamina structure and reservoir quality in shale oil reservoir of Fengcheng Formation in Mahu Sag. China. Mar. Petrol. Geol. 133, 105299.

Wang, S., Wang, G., Li, D., Wu, X., Chen, X., Wang, Q., Cao, J., Zhang, Y., 2022. Comparison between double caliper, imaging logs, and array sonic log for determining the in-situ stress direction: a case study from the ultra-deep fractured tight sandstone reservoirs, the Cretaceous Bashijiqike Formation in Keshen8 region of Kuqa depression, Tarim Basin, China. Petrol. Sci. 19 (6), 2601–2617.

Wilson, T.H., Smith, V., Brown, A., 2015. Developing a model discrete fracture network, drilling, and enhanced oil recovery strategy in an unconventional naturally fractured reservoir using integrated field, image log, and threedimensional seismic data. AAPG (Am. Assoc. Pet. Geol.) Bull. 99 (4), 735–762.

Wu, S., Yang, Z., Pan, S., Cui, J., Lin, S., Su, L., Bale, H., Hong, Y., Shi, W., 2020. Three-dimensional imaging of fracture propagation in tight sandstones of the upper triassic Chang 7 member, Ordos Basin, northern China. Mar. Petrol. Geol. 120, 104501.

Xi, K., Cao, Y., Lin, M., Niu, X., Zhu, R., Wei, X., You, Y., Liang, X., Feng, S., 2020. Laminae combination and shale oil enrichment patterns of Chang 73 sub-member organic-rich shales in the Triassic Yanchang Formation, Ordos Basin, NW China. Petrol. Explor. Dev. 47 (6), 1342–1353.

Xu, K., Yang, H., Zhang, H., Ju, W., Li, C., Fang, L., Wang, Z., Wang, H., Yuan, F., Zhao, B., Zhang, W., Liang, J., 2022. Fracture effectiveness evaluation in ultra-deep reservoirs based on geomechanical method, Kuqa Depression, Tarim Basin, NW China. J. Petrol. Sci. Eng. 215, 110604.

Xu, S., Tang, X., Torres-Verdín, C., et al., 2018. Seismic shear wave anisotropy in cracked rocks and an application to hydraulic fracturing. Geophys. Res. Lett. 45 (11), 5390–5397.

Xu, S., Gou, Q., Hao, F., Zhang, B., Shu, Z., Zhang, Y., 2020. Multiscale faults and fractures characterization and their effects on shale gas accumulation in the Jiaoshiba area, Sichuan Basin, China. J. Petrol. Sci. Eng. 189, 107026.

Yang, Z., Wang, X., Ge, H., Zhu, J., Wen, Y., 2022. Study on evaluation method of fracture forming ability of shale oil reservoirs in Fengcheng Formation, Mahu sag. J. Petrol. Sci. Eng. 215, 110576.

Zhang, J., Yu, Q., Li, Y., Pan, Z., Liu, B., 2023. Hydraulic fracture vertical propagation mechanism in interlayered brittle shale formations: an experimental investigation. Rock Mech. Rock Eng. 56 (1), 199–220.

Zhang, S., Yan, J., Cai, J., Zhu, X., Hu, Q., Wang, M., Geng, B., Zhong, G., 2021. Fracture characteristics and logging identification of lacustrine shale in the jiyang depression, bohai bay basin, eastern China. Mar. Petrol. Geol. 132, 105192.

Zhao, J., Yong, R., Hu, D., She, C., Fu, Y., Wu, J., Jiang, T., Ren, L., Zhou, B., Lin, R., 2024. Deep and ultra-deep shale gas fracturing in China: problems, challenges and directions. Acta Pet. Sin. 45 (1), 295–311.

Zou, C., Pang, S., Jing, Z., Gao, J., Yang, Z., Wu, S., Zhao, Q., 2020. Shale oil and gas revolution and its impact. Acta Pet. Sin. 41 (1), 1–12.

Zou, Y., Zhang, S., Ma, X., Zhou, T., Zeng, B., 2016. Numerical investigation of hydraulic fracture network propagation in naturally fractured shale formations. J. Struct. Geol. 84, 1–13.

Zeng, L., Li, X., 2009. Fractures in sandstone reservoirs with ultra-low permeability: a case study of the upper triassic Yanchang Formation in the Ordos Basin, China. AAPG (Am. Assoc. Pet. Geol.) Bull. 93 (4), 461–477.

Zeng, L., Song, Y., Liu, G., Tan, X., Xu, X., Yao, Y., Mao, Z., 2023. Natural fractures in ultra-deep reservoirs of China: a review. J. Struct. Geol. 175, 104954.